

# Watching the precession of a single nuclear spin by weak measurements

K. S. Cujia, J. M. Boss, J. Zopes, and C. L. Degen

*Department of Physics, ETH Zurich, Otto Stern Weg 1, 8093 Zurich, Switzerland*

(Dated: April 19, 2022)

Nuclear magnetic resonance (NMR) spectroscopy is a powerful technique for analyzing the structure and function of molecules, and for performing three-dimensional imaging of the spin density. At the heart of NMR spectrometers is the detection of electromagnetic radiation, in the form of a free induction decay (FID) signal<sup>1</sup>, generated by nuclei precessing around an applied magnetic field. While conventional NMR requires signals from  $10^{12}$  or more nuclei, recent advances in sensitive magnetometry<sup>2,3</sup> have dramatically lowered this number to a level where few or even individual nuclear spins can be detected<sup>4-8</sup>. It is natural to ask whether continuous FID detection can still be applied at the single spin level, or whether quantum back-action modifies or even suppresses the NMR response. Here we report on tracking of single nuclear spin precession using periodic weak measurements<sup>9</sup>. Our experimental system consists of a  $^{13}\text{C}$  nuclear spin in diamond that is weakly interacting with the electronic spin of a nearby nitrogen-vacancy center, acting as an optically readable meter qubit. We observe and minimize two important effects of quantum back-action: Measurement-induced decoherence<sup>10</sup> and frequency synchronization with the sampling clock<sup>11</sup>. We use weak measurements to demonstrate nanoscale NMR spectroscopy with a simultaneous enhancement of the signal-to-noise ratio (SNR), frequency bandwidth and spectral resolution. Our method may provide the optimum route for performing single-molecule NMR<sup>12-14</sup> at atomic resolution.

Measurement back-action, an important feature of quantum measurements<sup>15,16</sup>, can usually be neglected in NMR because the spin-detector coupling is extremely weak. One prominent exception is radiation damping<sup>17</sup>, where the collective coupling of the nuclear ensemble gives rise to a damping of the magnetic resonance by the electric detection circuit. As nuclear ensembles become smaller, eventually consisting of only few or even a single nuclear spin, the close coupling to the detector is expected to modify<sup>18,19</sup> or inhibit<sup>20</sup> the free evolution of the spin. Recent work on ensembles of trapped ions<sup>10</sup> reported simultaneous tracking of spin angle and amplitude through the use of weak, quantum-non-demolition measurements, indicating an avenue for mitigating back-action. Here, we show that it is possible to continuously track the free precession of a single nuclear spin.

To probe the coherent precession of a single nuclear spin we devised the measurement system depicted in Fig.

1a. Our system consists of a  $^{13}\text{C}$  nucleus (spin  $I = 1/2$ ) isolated in the nearly spin-free lattice of a diamond crystal. The nuclear spin undergoes a free precession around the Z axis with an angular velocity given by the Larmor frequency  $\omega_0 = -\gamma_n B_0$ , where  $B_0$  is the local magnetic field and  $\gamma_n$  the nuclear gyromagnetic ratio. To detect the nuclear precession, we periodically couple the nuclear spin to the electronic spin of a nearby NV center acting as an optically readable meter qubit. We monitor the precession by probing the nuclear  $\hat{I}_x$  spin component by means of a conditional rotation, via the interaction Hamiltonian  $\hat{H}_{\text{meas}} = g 2\hat{I}_x \hat{S}_z$ , where  $g$  is a coupling constant. For two-spin systems this Hamiltonian can be realized, for instance, by a Carr-Purcell-type dynamical decoupling sequence applied to the meter spin<sup>21,22</sup>. The interaction with the nuclear spin imprints a signal proportional to  $\sin(\beta)\langle\hat{I}_x\rangle$  onto the optically measurable  $\hat{S}_z$  spin component of the meter, where  $\beta = gt_\beta$  is the rotation angle that determines the measurement strength<sup>23</sup>. Importantly, by varying the interaction time  $t_\beta$ , we can smoothly tune the strength of the measurement, or turn it off completely. This feature allows us to explore the cross-over from the strong ( $\beta \approx \pi/2$ ) to the weak ( $\beta \rightarrow 0$ ) measurement regime.

In addition to providing the signal, the interaction with the meter also modifies the trajectory of the nuclear evolution, leading to back-action. The state evolution is illustrated in Fig. 1c and can be sequenced into two unitary rotations and a partial projection<sup>23</sup>: During each sampling interval, (i) the nuclear spin angle  $\phi$  accumulates a free precession phase  $\alpha = \omega_0 t_s$ , where  $t_s$  is the dwell time. (ii) The interaction with the meter qubit rotates the nuclear spin around the X axis by the angle  $\pm\beta$ , where the sign is conditional on the  $\hat{S}_z$  state of the meter. (iii) Projective optical readout of the meter  $\hat{S}_z$  component collapses the nuclear vector onto the XY plane, which reduces the amplitude of the  $\hat{I}_y$  component by a factor of  $\cos(\beta)$  and gives a small phase kickback  $\delta \approx -\frac{1}{4}\beta^2 \sin(2\phi)$  to the spin angle  $\phi$ . Under precession,  $\hat{I}_x$  and  $\hat{I}_y$  alternate roles as the measured and perturbed variables, leading to an exponential decay of the spin amplitude with a decay rate  $\Gamma_\beta \approx \beta^2/(4t_s)$  and an average precession rate  $\langle\omega\rangle := \langle d\phi/dt\rangle \approx \omega_0$ . By plotting the meter output as a function of readout index  $n$ , we therefore expect a decaying oscillation, allowing us to extract estimates for the precession frequency  $\omega_0$  and the decay rate  $\Gamma$ . Importantly, by making the measurement weak (small  $\beta$ ), we can quadratically suppress measurement-induced decoherence  $\Gamma_\beta \propto \beta^2$  while only linearly reducing the signal amplitude  $A \propto \beta$ .

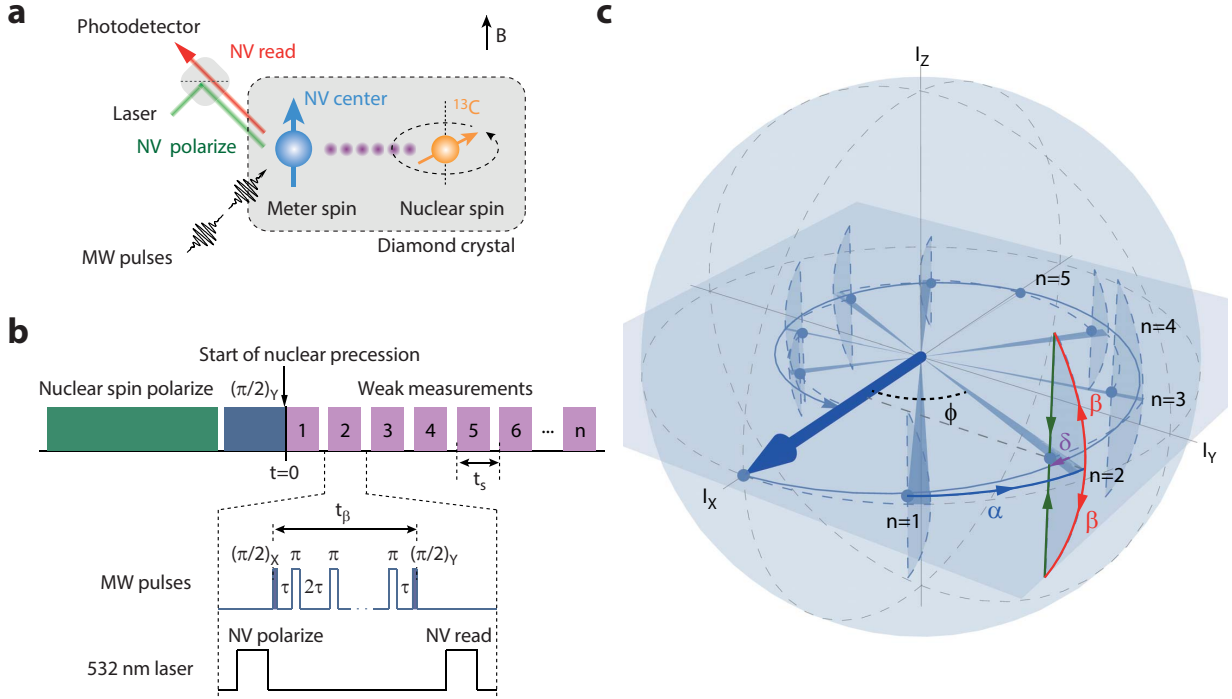


**FIG. 1. Scheme for tracking of single nuclear spin precession.** **a**, Measurement system: A meter qubit, implemented by the electronic spin of a single NV center in diamond, weakly probes a precessing  $^{13}\text{C}$  nuclear spin. The meter is read out via a strong optical measurement. The interaction between electronic and nuclear spins can be turned on and off by microwave manipulation of the electronic spin. **b**, Measurement protocol: The nuclear spin is polarized into  $\hat{I}_z$  (green) and rotated by  $\pi/2$  (blue) to initiate precession. Weak measurements (purple) are implemented by a conditional rotation of the electronic-nuclear spin pair followed by an optical readout of the NV spin component  $\hat{S}_z$ . We implement the conditional rotation as a decoupling sequence of periodically spaced  $\pi$  pulses (inset) where  $\tau \sim \pi/(2\omega_0)$ . To track the nuclear precession, weak measurements are repeated at instances of the sampling time  $t_s$ . **c**, Bloch-sphere representation of the nuclear state evolution. At  $t = 0$  the nuclear vector points along the  $+X$  axis (bold arrow). A Z-oriented magnetic field  $B_0$  drives spin precession in the XY plane. Each sampling interval consists of (i) an advance of the spin vector  $\phi$  by the angle  $\alpha = \omega_0 t_s$  (modulo  $2\pi$ ) due to free precession (blue arrow), a conditional rotation around the  $\pm X$  axes by  $\beta$  (red arrows), and a strong readout of the electronic sensor qubit causing projection of the nuclear spin onto the XY plane (green arrows). Each weak measurement reduces the amplitude of the  $\hat{I}_y$  component by  $\cos(\beta)$  and gives a phase kick  $\delta$  (purple arrow) to the spin angle. Periodic weak measurements of the nuclear spin produce an inward spiraling precession trace.

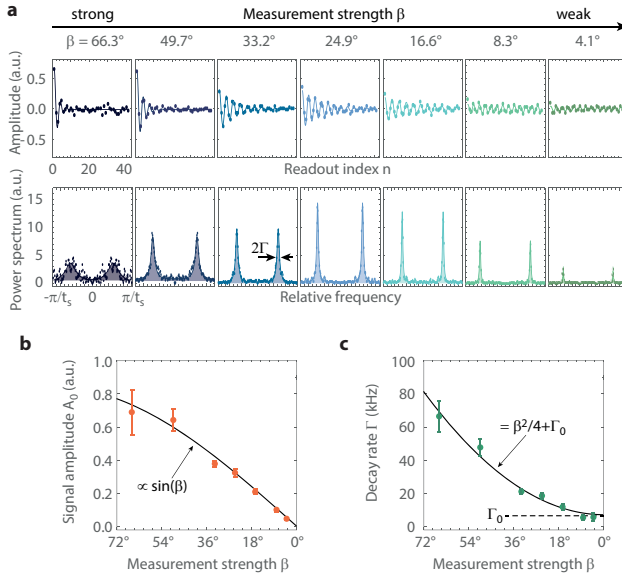


**FIG. 2. Experimental observation of single  $^{13}\text{C}$  precession.** **a**, Time traces (upper panels) and corresponding power spectra (lower panels) for decreasing measurement strengths  $\beta$ . We vary  $\beta$  by adjusting the interaction time  $t_\beta$  from 3.9 to 0.25  $\mu\text{s}$ . The dots show the experimental data and the solid lines are fits to exponentially decaying sinusoids (time traces) and Lorentzians (power spectra). The spectra are obtained from undersampled time traces and are plotted on a relative frequency scale. **b**, Signal amplitudes  $A_0$  as a function of measurement strength  $\beta$ . The dots depict the fit results from (a). The solid curve is the function  $\sin(\beta)$  that is vertically scaled to fit the data. **c**, Decay rates  $\Gamma$  as a function  $\beta$ . The dots depict the fit results from (a). The solid curve is the function  $\beta^2/4 + \Gamma_0$ , where  $\Gamma_0$  accounts for the intrinsic nuclear dephasing with a decay time  $T_{2,n}^* = (\Gamma_0)^{-1} = 134 \mu\text{s}$ .

Experimental traces of single  $^{13}\text{C}$  spin precession are shown in Fig. 2. Seven experiments are plotted where the measurement strength  $\beta$  decreases from left to right. We control  $\beta = gt_\beta$  through the interaction time  $t_\beta$ , where the coupling  $g = 2\pi \cdot 46.8 \text{ kHz} \approx a_\perp/\pi$  is set by the transverse hyperfine coupling parameter  $a_\perp$  between the electronic and nuclear spin<sup>22</sup>.  $a_\perp$  is determined by an independent calibration<sup>23</sup>. For all measurements, the nuclear spin is initially polarized into the  $\hat{I}_z$  state by repetitive initialization and rotated into  $\hat{I}_x$  to initiate precession (see Methods). The nuclear evolution is then tracked by periodically probing  $\hat{I}_x$  at instances of the sampling time  $t_s$ . The measurement output is the photon count of the NV meter spin, averaged over  $\sim 10^6$  repetitions of the experiment to reach adequate SNR.

The experiment of Fig. 2a clearly demonstrates that the free precession of a single nuclear spin can be continuously tracked, and that we can minimize back-action by simply reducing the measurement strength  $\beta$ : When probing  $\hat{I}_x$  strongly ( $\beta = 66.3^\circ$ ), the oscillation collapses within a few measurement cycles. Conversely, when using weak measurements ( $\beta = 4.1^\circ$ ), the oscillation persists over the entire measurement record with little de-

lay. By fitting each trace to an exponentially decaying oscillation, we can extract the signal amplitudes and decay rates (Fig. 2c,d). As expected, the signal amplitude  $A_0 \propto \sin \beta \approx \beta$  for small  $\beta$  while the decay rate  $\Gamma \propto \beta^2/4 + \Gamma_0$ . The offset  $\Gamma_0$  represents the intrinsic dephasing of the nuclear spin,  $\Gamma_0 = (T_{2,n}^*)^{-1}$ , caused in our experiments either by a residual hyperfine interaction to the NV center or by slow drifts in the static magnetic bias field (see Methods).

We next address the question of whether the continuous weak observation of the nuclear spin alters the free precession frequency, which is the most important quantity in NMR spectroscopy. Our experimental estimate for the precession frequency  $\langle \omega \rangle$  is the time derivative of the spin angle averaged over one time trace. We extract  $\langle \omega \rangle$  by fitting the peak position in the power spectrum (see Fig. 2a). To analyze whether  $\langle \omega \rangle$  corresponds to the “true” free precession frequency  $\omega_0$ , we record a set of time traces for varying forward precession angles  $\alpha = (0.5 \dots 2.5)\pi$ . We tune  $\alpha = \omega_0 t_s$  by incrementing the sampling time  $t_s$  over one Larmor period. Fig. 3a shows the resulting power spectra (vertical axis) as a function of precession angle  $\alpha$  (horizontal axis) in a normalized color plot. Clearly, the peaks appear at the diagonal positions where  $\langle \omega \rangle t_s = \alpha$ . A statistical analysis of the peak frequencies confirms that  $\langle \omega \rangle t_s$  and  $\alpha$  agree within the experimental error<sup>23</sup>. Fig. 3a demonstrates that, in general, weak measurements do not modify the free precession frequency.

Although Fig. 3a suggests that  $\langle \omega \rangle t_s = \alpha$  for all values of  $\alpha$ , a closer inspection reveals that the equality is violated near the cross-over points where  $\alpha = k\pi$ ;  $k \in \mathbb{N}$  is a multiple of  $\pi$  (white boxes). As  $\alpha \rightarrow k\pi$  (Fig. 3b), the precession rate  $\langle \omega \rangle$  abruptly locks to the fixed value of  $\pi/t_s$ , meaning that the precession synchronizes with the sampling clock. This synchronization becomes more pronounced as the measurement strength is increased (Fig. 3b, top to bottom). The phenomenon can be explained by the phase kickback  $\delta$  of the weak measurement (purple arrow in Fig. 1c): Because  $\hat{I}_y$  is scaled while  $\hat{I}_x$  is not, the spin vector is effectively squeezed towards the X axis. Once the forward precession angle becomes smaller than the maximum kickback,  $\text{mod}(\alpha, \pi) < \delta_{\text{max}} = \beta^2/4$ , the spin vector is trapped and synchronization sets in. This explanation is supported by the excellent agreement of the theoretical description (Methods) with our experimental observations and complementary density matrix simulations (Fig. 3c).

Frequency synchronization leads to several intriguing features that we only briefly sketch out. First, the phase locking stabilizes the precession and suppresses dephasing of the nuclear spin (Fig. 3c). This suppression is strongest for  $\alpha = \pi$  since the spin vector is always close to the X axis, and less effective once  $\alpha$  moves away from  $\pi$ . Second, the synchronization leads to a spontaneous initialization into  $\pm \hat{I}_x$  from a random spin orientation (Fig. 3d). Note that our observed frequency synchronization, while reminiscent of the quantum Zeno effect<sup>24</sup>,

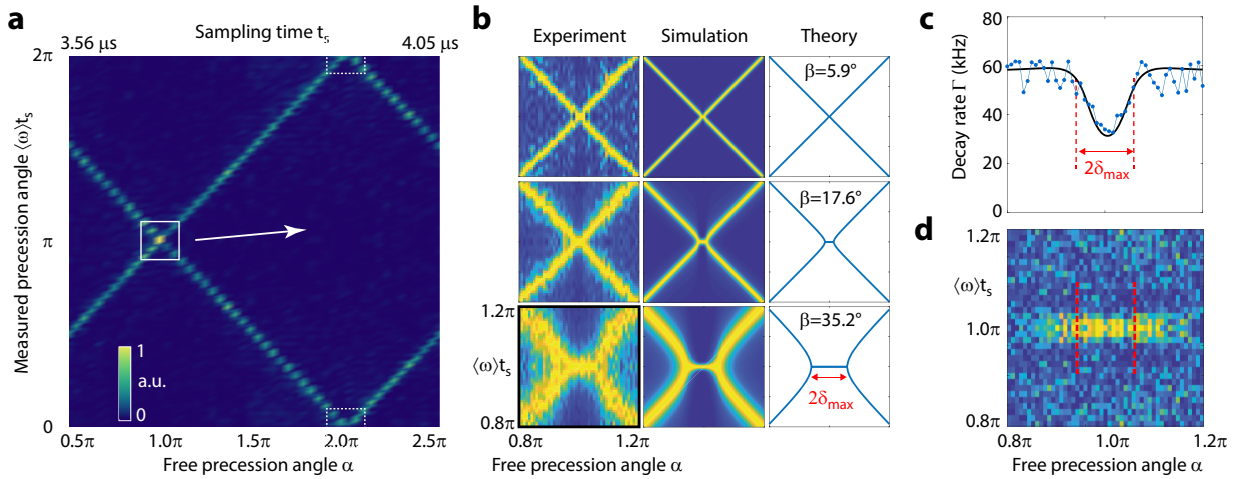


**FIG. 3. Frequency synchronization.** **a**, Normalized power spectra (vertical axis) plotted as a function of the free precession angle  $\alpha$  (horizontal axis). We vary  $\alpha$  by incrementing the sampling time from  $3.56 \mu\text{s}$  to  $4.05 \mu\text{s}$  in steps of  $10 \text{ ns}$ . The peak positions in the power spectra identify the average precession angle  $\langle \omega \rangle t_s$ . **b**, Zoom into the region  $\alpha = 0.8\ldots 1.2\pi$  showing frequency synchronization. The locking range  $2\delta_{\max} = \beta^2/2$  increases with the square of the measurement strength  $\beta$  (top to bottom). The left panels show the experimental observation, the middle panels show a density matrix simulation, and the right panels show the theoretical expectation (see Methods). **c**, Nuclear dephasing rate  $\Gamma$  plotted as a function of  $\alpha$ , revealing suppressed dephasing under synchronization. **d**, Spontaneous alignment of the nuclear spin. The plot shows the same measurement as in (b), bottom row, recorded without prior initialization of the nuclear spin. Under synchronization, the nuclear spin spontaneously aligns with  $\hat{I}_x$  leading to a bright signal peak. No peak is observed in the non-synchronized regime. The measurement strength in (a) is  $\beta = 8.6^\circ$ . The measurement strength in (c,d) is  $\beta = 35^\circ$  and the locking range is  $2\delta_{\max} = 0.06\pi$ .

is more closely related to the concept of atomic phase locking<sup>11,25</sup> and the phenomenon of spin locking in magnetic resonance<sup>26</sup>.

We finally show that the continuous tracking of spin precession extends our ability to detect very weakly coupled nuclear spins, and will lead to new capabilities in nanoscale NMR spectroscopy and imaging. First, continuous weak measurements can efficiently probe weakly coupled nuclei where strong measurements are no longer possible because of sensor decoherence. Fig. 4 shows the NMR spectrum of a  $^{13}\text{C}$  nucleus whose coupling constant  $g/(2\pi) = 4.6 \text{ kHz}$  is less than the decoherence rate  $T_{2,\text{CP}}^{-1} = 6.1 \text{ kHz}$  of the meter spin. Although in this case  $g$  is not much smaller than  $T_{2,\text{CP}}^{-1}$ , we find that weak measurements maintain a constant SNR down to very small couplings  $g > (T_{2,\text{n}}^*)^{-1}$ , limited only by the intrinsic dephasing of the nuclear spin<sup>23</sup>. Second, weak continuous measurements simultaneously open up the meter's frequency bandwidth, which is set by the inverse of the interaction time  $t_\beta^{-1}$  (Fig. 4b). Since  $t_\beta$  can be made very short, a broad window of NMR resonance can be covered. Third, continuous sampling protocols are not subject to linewidth limitations imposed by the relaxation times  $T_1$  and  $T_2$  of the meter qubit<sup>30-32</sup>, allowing one to achieve an NMR-limited frequency resolution.

In summary, we have shown that the Larmor precession of a single nuclear spin can be continuously tracked, and that back-action can be almost completely avoided by making measurements sufficiently weak. Our experi-

ments give deep insight into the quantum dynamics of the measurement, as revealed by the emergence of frequency synchronization at near commensurate sampling. Our results open the way to extending NMR spectroscopy to very weakly coupled nuclear spins and spin clusters<sup>33,34</sup>, with a simultaneous enhancement of the spectral resolution, spectral bandwidth, and SNR. The method is compatible with hyperpolarization techniques<sup>35,36</sup>, which will further improve the sensitivity, a key limitation in nanoscale NMR. The method can further be combined with advanced NMR pulse schemes, which can be interspersed with the weak measurements and provide internuclear distances and bonding information. Although many technical issues still remain, the prospect for three-dimensional imaging of single molecules with atomic resolution and chemical selectivity provides a strong motivation for exploring these possibilities.

**Acknowledgments:** This work has been supported by the Swiss National Science Foundation through project grants 200020\_156100, 200020\_175600 and through the NCCR QSIT, and by the European Commission through DIADEMS grant 611143. We thank Renbao Liu, Alex Retzker and Tim Taminiau for helpful discussions, Kevin Chang for experimental support, and Marius Palm and Konstantin Herb for proof-reading the manuscript.

**Author contributions:** C.L.D. conceived the project. K.S.C. and J.M.B. carried out the experiments

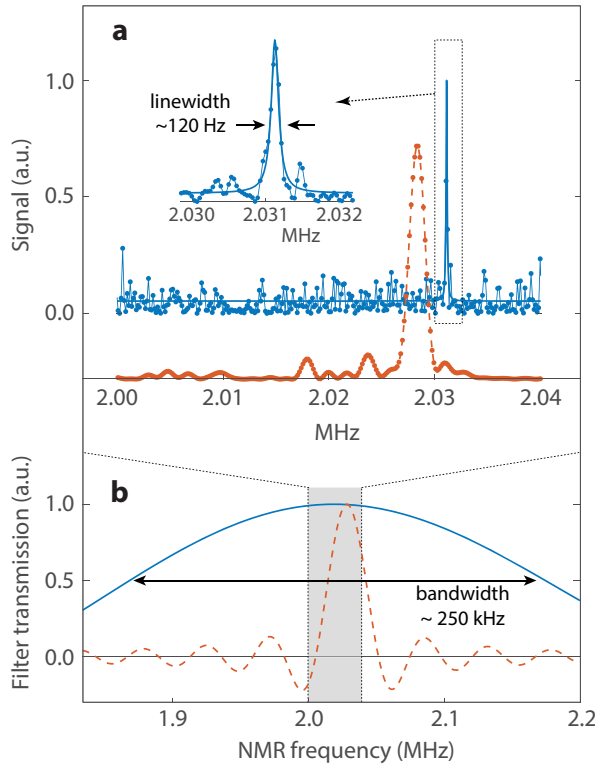


**FIG. 4. NMR spectroscopy of a weakly coupled  $^{13}\text{C}$ .** **a**, Experimental NMR spectrum (in blue) of a single  $^{13}\text{C}$  nuclear spin recorded in a bias field of  $B_0 \approx 190.2$  mT, obtained from a 7 ms-long time trace of 501 weak measurements. The spectral resolution (inset) is obtained by fitting to a Lorentzian line shape and is limited by residual drifts in the bias field. For comparison, we have also recorded a conventional correlation spectrum<sup>22,27</sup> in a bias field  $B_0 \approx 189.8$  mT based on a strong measurement (in red, offset for clarity). For this NV center,  $T_{2,\text{CP}} \sim 165$   $\mu\text{s}$  and  $T_1 \sim 2$  ms. **b**, Frequency bandwidth of the continuous weak measurement (solid blue line). The plot shows the filter function<sup>28,29</sup> of the dynamical decoupling sequence (see Fig. 1b), corresponding to the NMR frequency range over which the conditional rotation is effective. The bandwidth (full width at half maximum) is approximately  $t_\beta^{-1} = (3.94 \mu\text{s})^{-1} = 254$  kHz. The much narrower bandwidth for the corresponding strong measurement (red dotted line) is  $t_\beta^{-1} = (43.4 \mu\text{s})^{-1} = 23$  kHz.

with the support of J.Z and analyzed the data. K.S.C., C.L.D. and J.M.B. performed the simulation and theoretical analysis of weak measurements. All authors discussed the results and participated in writing the manuscript.

## Methods

**Diamond samples:** Two single-crystal diamond chips were used for experiments. Sample A (NV1, NV3, NV4, NV5) was an electronic-grade, natural abundance (1.1%  $^{13}\text{C}$ ) diamond membrane. We etched nano-pillars<sup>37,38</sup> into the membrane surface to increase

the photon collection efficiency. Sample B (NV2) was an unstructured diamond chip overgrown with 20 nm of enriched  $^{12}\text{C}$  (99.99%), 1 nm of enriched  $^{13}\text{C}$  (estimated in-grown concentration  $\sim$ 5-10%), and a 5 nm cap of enriched  $^{12}\text{C}$  (99.99%); further details on the sample are given in Ref.<sup>39</sup> (“Sample B”). NV centers in both samples were created by  $^{15}\text{N}^+$  ion implantation at an energy of 5 keV and subsequent annealing at 850° C. We chose the  $^{15}\text{N}$  species to discriminate implanted NV centers from native ( $^{14}\text{N}$ ) NV centers. Both samples were cleaned in a 1:1:1 mixture of  $\text{H}_2\text{SO}_4:\text{HNO}_3:\text{HClO}_4$  and baked at 465° C before mounting them in the setup. The continuous wave (CW) photon count rate was between 250 and 700 kC/s for sample A and between 40 and 50 kC/s for sample B.

**Experimental setup:** Experiments were performed with a custom-built confocal microscope equipped with a green 532 nm excitation laser and a 630 – 800 nm detection path using a single photon detector. Optical pulses were generated by an acousto-optic modulator and gating of arriving photons was realized by time-tagging and software binning of photon counts. Microwave pulses for manipulating the electronic spin were synthesized using an arbitrary waveform generator (Tektronix AWG5012C), up-converted to  $\sim$  2.5 GHz using a local oscillator (Hittite HMCT2100) and a single-sideband mixer (IQ1545, Marki microwave) and subsequently amplified (Gigatronics GT-1000A). The pulses were delivered to the NV center using a coplanar waveguide defined on a quartz cover slip by photolithography. The transmission line was terminated on an external  $50 \Omega$  load.

We used a cylindrical permanent magnet to create a magnetic bias field of  $\sim$  190 mT at the location of the NV center. We aligned the magnetic field direction with the NV symmetry axis by adjusting the relative location of the permanent magnet. The alignment was optimized by fitting to a set of EPR lines recorded at different magnet locations and by maximizing the CW photon count rate.

**Tracking of magnetic field drifts:** For long acquisition times ( $\sim$  hours), the magnetic bias field drifted by typically a few Gauss, leading to variations in the EPR frequency of a few MHz and variations in the  $^{13}\text{C}$  Larmor frequency of a few kHz. These drifts were likely caused by a temperature-related change of the magnetization of the permanent magnet providing the bias field. We continuously tracked and logged the field drift during a measurement via the EPR resonance of the NV center. We adjusted the microwave excitation frequency in real time, and used post-correction<sup>40</sup> to compensate for the drift in the  $^{13}\text{C}$  spectrum. The residual drift was on the order of 30-50 ppm.

**Detection protocol:** A detailed diagram of the detection protocol is given in Supplementary Fig. 1. The protocol consisted of three steps: (i) Polarization of the

nuclear spin, (ii) a  $90^\circ$  pulse to initiate the free nuclear precession, and (iii) a series of  $n$  weak measurements.

*Polarization:* To polarize the nuclear spin, we followed the method of Ref. 21. We first initialized the electronic spin into  $m_S = 0$  using a laser pulse. We then applied a conditional nuclear  $\pi/2$  X rotation, implemented as a resonant Carr-Purcell-Meiboom-Gill (CPMG) decoupling sequence applied to the electronic spin. We next applied a nuclear  $\pi/2$  Z rotation, implemented as a waiting time of duration  $\tau$ . We then applied a second conditional nuclear  $\pi/2$  X rotation, implemented by another CPMG sequence with the initial and final electronic  $\pi/2$  pulses omitted. We finally applied a laser pulse to repolarize the electronic spin into  $m_S = 0$ . We typically repeated this sequence a few times until the polarization was well above 50% (see Supplementary Fig. 2).

*Nuclear 90° pulse:* The nuclear  $\pi/2$  Y rotation was applied by means of another resonant CPMG sequence, again with the initial and final electronic  $\pi/2$  pulses omitted.

*Weak measurements:* The weak measurements were implemented by polarizing the electronic spin into  $m_S = 0$  using a laser pulse, applying a resonant CPMG sequence of duration  $t_\beta$ , and reading out the electronic state with a second laser pulse. To obtain a meter output that is proportional to  $\hat{I}_x$ , the initial and final electronic  $\pi/2$  pulses of the CPMG sequence must be phase shifted by  $90^\circ$  with respect to each other<sup>31</sup>.

**Calibration of electronic and nuclear spin parameters:** The resonance frequency of the electronic spin was calibrated by an optically-detected magnetic resonance spectroscopy scan. The nuclear Larmor frequency  $\omega_0$  as well as the parallel and transverse hyperfine coupling parameters ( $a_{||}$  and  $a_{\perp}$ ) were calibrated using correlation spectroscopy<sup>22</sup>. The reported coupling constants  $g$  are equal to  $\pi/(2t_\beta)$  where  $t_\beta$  is the CPMG duration leading to a  $\beta = \pi/2$  rotation. All calibration data are provided as Supplementary Information.

**Derivation of the measurement-induced decay rate:** Assume that after  $n$  weak measurements the spin vector has length  $r_n < 1$ . Then, the length  $r_{n+1}$  after the  $(n+1)$ 'th weak measurement is  $r_{n+1} = \sqrt{1 - \sin \phi^2(1 - \cos \beta^2)}r_n$ , where  $\phi$  is the instantaneous spin angle just before the measurement and  $\beta$  is the angle of the conditional rotation. If  $\beta \ll \pi/2$  is small, we find  $r_{n+1} \approx \cos(\beta \sin \phi)r_n$ . For a series of  $n$  weak measurements at spin angles  $\phi$  uniformly distributed between 0 and  $2\pi$ ,  $r_n \approx \langle \cos(\beta \sin \phi) \rangle^n \approx \exp(-n\beta^2/4) \approx \exp(-\Gamma_\beta t)$ , where the average is over  $\phi = 0 \dots 2\pi$  and where

$$\Gamma_\beta = \beta^2/(4t_s) \quad (1)$$

is the exponential decay rate. A quantum mechanical derivation of Eq. (1) is given in Supplementary Note 1.

**Derivation of frequency synchronization:** The phase kick  $\delta$  is given by the difference of the spin angle before and after a weak measurement. Using the simple geometric picture of rotations on the Bloch sphere (Fig. 1c) we find that  $\delta = \arctan(\tan \phi \cos \beta) - \phi$ . Reforming this expression into  $\tan(\phi + \delta) = \tan \phi \cos \beta$  and applying the tangent's sum rule, we find

$$\tan \delta = -\frac{\tan \phi(1 - \cos \beta)}{1 + \tan \phi^2 \cos \beta} \approx -\frac{\beta^2}{4} \sin 2\phi \quad (2)$$

where the approximation holds for small  $\beta \ll \pi/2$ . Eq. (2) shows that: (i) the phase kick is independent of the sign of  $\beta$ , thus both projections of the electronic spin generate the same kick, (ii) the phase kick alternates direction on each quadrant since  $\sin(2\phi)$  changes sign every  $90^\circ$ , (iii) therefore, frequency synchronization is expected when the free precession angle  $\alpha$  is an integer multiple of  $\pi$ , and (iv) the maximum phase kick is  $|\delta_{\max}| \approx \beta^2/4$ , defining the locking range for synchronization. Eq. (2) further determines the steady-state spin angle  $\phi_{ss}$  under synchronization, found by setting  $\delta = -\alpha$  (modulo  $\pi$ ) and solving for  $\phi$ :

$$\phi_{ss} = \frac{1}{2} \sin^{-1} \left[ \frac{4 \tan \alpha}{\beta^2} \right] \approx \frac{2\alpha}{\beta^2} \quad (3)$$

where the last expression is for small  $\phi_{ss} \ll \pi/4$ .

Frequency synchronization suppresses nuclear dephasing both because measurement-induced decoherence is reduced, and because Z phase noise is canceled by the phase kickback  $\delta$ . The measurement-induced decoherence is reduced because the spin vector is always close to  $\hat{I}_x$ , which is not disturbed by the weak measurement. For reasonably small  $\phi_{ss} \ll \pi/4$ , the decoherence rate is  $\Gamma_\beta^{\text{sync}} \approx 2\Gamma_\beta \sin^2 \phi_{ss} \approx \Gamma_\beta \alpha^2/(2\delta^2)$ , where  $\Gamma_\beta$  is given by Eq. (1) and  $\alpha$  is modulo  $\pi$ . Clearly,  $\Gamma_\beta^{\text{sync}}$  vanishes as  $\alpha \rightarrow 0$ . Frequency synchronization is also expected to suppress the intrinsic nuclear dephasing due to Z phase noise, however, we did not observe this effect in the present study.

We finally calculate the average precession frequency  $\langle \omega \rangle$  under weak continuous measurements for all values of the precession angle  $\alpha$ . Inside the locking range,

$$\langle \omega \rangle = \frac{k\pi}{t_s} \quad \text{if } \mod(\alpha, \pi) \leq \delta_{\max} \quad (4)$$

where  $k \in \mathbb{N}$  is determined by the undersampling. Outside the locking range, the instantaneous precession frequency at spin angle  $\phi$  is  $\omega(\phi) = (\alpha + \delta)/t_s = \omega_0 - \frac{\beta^2}{4t_s} \sin 2\phi = \omega_0 - \Gamma_\beta \sin 2\phi$ . The experimentally measured precession frequency  $\langle \omega \rangle$  is the time average of  $\omega(\phi)$ . We calculate  $\langle \omega \rangle$  by integrating over one full precession cycle  $T$ ,

$$\begin{aligned} \langle \omega \rangle &= \frac{2\pi}{T} = 2\pi \left[ \int_0^{2\pi} \frac{d\phi}{\omega(\phi)} \right]^{-1} \\ &= \omega'_0 \sqrt{1 - (\Gamma_\beta/\omega'_0)^2} \quad \text{if } \mod(\alpha, \pi) > \delta_{\max} \end{aligned} \quad (5)$$

where  $\omega'_0$  is equal to  $\omega_0$  modulo  $k\pi/t_s$ . Eq. (5) shows that  $\langle\omega\rangle$  diverges with the square of  $\alpha \propto \omega'_0$  as  $|\alpha| \geq \delta_{\max}$ , where  $\alpha$  is again modulo  $\pi$ .

**Intrinsic nuclear dephasing:** Contributing factors to the intrinsic nuclear dephasing rate  $\Gamma_0 = (T_{2,n}^*)^{-1}$  include:

*Dipolar broadening:* The dipolar coupling to surrounding  $^{13}\text{C}$  nuclei causes a homogeneous broadening of the magnetic resonance. This effect is expected to be  $< 50$  Hz in our system.

*Magnetic field drift:* Slow drifts in the static magnetic bias field cause fluctuations in the Larmor frequency, as discussed above. With frequency tracking, the contribution is on the order of 30-50 ppm, equivalent to  $50 - 100$  Hz.

*Residual hyperfine interaction during optical illumination:* During optical readout and re-initialization of the NV center via a non-resonant laser pulses, the NV center cycles through its electronic states until reaching the  $m_S = 0$  spin polarized steady state. During this process, the NV center stochastically jumps back and forth between spin states and possibly electronic charge states. This leads to random Z rotations of the nuclear spin due to the secular part of the hyperfine interaction  $a_{||} 2\hat{S}_z \hat{I}_z$ , where  $a_{||}$  is the parallel hyperfine coupling constant<sup>24</sup>. The random Z angle is  $\gamma \propto a_{||} t_{\text{readout}}$ , where  $t_{\text{readout}}$  is the duration during which  $m_S \neq 0$ . The length of the spin vector after  $n$  weak measurements is approximately  $\langle \cos \gamma \rangle^n = \exp(-n\langle \gamma^2 \rangle/2) = \exp(-\Gamma_\gamma t)$ , where  $\Gamma_\gamma \propto a_{||}^2 t_{\text{readout}}^2 / (2t_s)$ . For the measurements shown in Fig. 2, we obtain  $\Gamma_\gamma = 7.4$  kHz =  $(134 \mu\text{s})^{-1}$  using  $t_{\text{readout}} = 2.8 \mu\text{s}$  and the experimental parameters given in Supplementary Data 3.

**Data analysis:** The data in Fig. 2a were fitted by  $A(n) = A_0 e^{-\Gamma_n n} \sin(2\pi f_0 n + \phi_0)$  with  $A_0$ ,  $\Gamma_n = \Gamma t_s$ ,  $f_0$ , and  $\phi_0$  as free fit parameters (time traces) and by  $S(f) = S_0 \Gamma^2 / [(f^2 - f_0^2) + \Gamma^2] + S_1$  with  $\Gamma$ ,  $f_0$ ,  $S_0$  and  $S_1$  as free fit parameters (power spectra). The time traces were zero-padded 4× before calculating the power spectra. The

data in Fig. 2b were fitted by  $A_0(\beta) = a \sin(\beta)$ , with  $a$  as a free fit parameter. The data in Fig. 2c were fitted by  $\Gamma(\beta) = \frac{\beta^2}{4} + \Gamma_0$ , with  $\Gamma_0$  as a free fit parameter. The decay rates in Fig. 3c were extracted from the data plotted in Fig. 3b (bottom) using the same fit functions as in Fig. 2a. The filter functions shown in Fig. 4 represent the weighting function of the CPMG sequence, given by Eq. (67) of Ref. 29,

$$W(f) = \frac{\sin(\pi f t_\beta)}{\pi f t_\beta} \tan(\pi f \tau) \quad (6)$$

using the values for  $t_\beta$  and  $\tau$  given in the Supplementary Data 3. The bandwidth (full width at half maximum, FWHM) of this filter function is approximately  $t_\beta^{-1}$ . The spectra shown in Fig. 4 were obtained from undersampled time traces, unfolded to the correct frequency using the center frequency  $f_c = 1/(4\tau)$  of the filter function and the sampling frequency  $f_s = 1/t_s$ . The spectra were zero padded 4× (weak measurement spectrum) and 10× (correlation spectrum) before applying the Fourier transformation. The reported linewidth is the FWHM of the power spectrum, and was extracted by fitting the spectrum to the function  $S(f) = (1 - S_0) \Gamma^2 / [(f - f_0)^2 + \Gamma^2] + S_0$ .

**Density matrix simulations:** To verify that our theory accurately describes the experimental results, we performed density matrix simulations of the coupled electron-nuclear two-spin system. We initialized the density matrix into the  $\sigma = (\hat{S}_z + \hat{S}_e) \otimes (\hat{I}_e + \hat{I}_x)$  state and calculated the evolution under  $n$  weak measurements. For each weak measurement, we applied a unitary evolution under the CPMG sequence, traced out the electronic spin states leaving only the nuclear spin part  $\sigma_I$  of the density matrix, and reinitialized the density matrix into  $\sigma = (\hat{S}_z + \hat{S}_e) \otimes \sigma_I$ . The value plotted in Fig. 3b is the expectation value  $\hat{S}_z$  of the electronic spin and we verified that  $\hat{S}_z \propto \hat{I}_x$ . The simulations used the experimental parameters listed in the Supplementary Data 3 as an input. The simulations did not account for finite pulse durations and spin relaxation.

<sup>1</sup> Hahn, E. L. Spin echoes. *Phys. Rev.* **80**, 580–594 (1950). URL <http://link.aps.org/doi/10.1103/PhysRev.80.580>.

<sup>2</sup> Poggio, M. & Degen, C. L. Force-detected nuclear magnetic resonance: Recent advances and future challenges. *Nanotechnology* **21**, 342001 (2010). URL <http://dx.doi.org/10.1088/0957-4484/21/34/342001>.

<sup>3</sup> Wrachtrup, J. & Finkler, A. Single spin magnetic resonance. *J. Magn. Reson.* **269**, 225–236 (2016).

<sup>4</sup> Jelezko, F. *et al.* Observation of coherent oscillation of a single nuclear spin and realization of a two-qubit conditional quantum gate. *Phys. Rev. Lett.* **93**, 130501 (2004). URL <https://link.aps.org/doi/10.1103/PhysRevLett.93.130501>.

<sup>5</sup> Mamin, H. J. *et al.* Nanoscale nuclear magnetic resonance with a nitrogen-vacancy spin sensor. *Science* **339**, 557–560 (2013).

<sup>6</sup> Staudacher, T. *et al.* Nuclear magnetic resonance spectroscopy on a (5-nanometer)(3) sample. *Science* **339**, 561–563 (2013).

<sup>7</sup> Loretz, M., Pezzagna, S., Meijer, J. & Degen, C. L. Nanoscale nuclear magnetic resonance with a 1.9-nm-deep nitrogen-vacancy sensor. *Appl. Phys. Lett.* **104**, 033102 (2014). URL <http://dx.doi.org/10.1063/1.4862749>.

<sup>8</sup> Muller, C. *et al.* Nuclear magnetic resonance spectroscopy with single spin sensitivity. *Nature Commun.* **5**, 4703–4703 (2014).

<sup>9</sup> (2014).

<sup>9</sup> Clerk, A. A., Devoret, M. H., Girvin, S. M., Marquardt, F. & Schoelkopf, R. J. Introduction to quantum noise, measurement, and amplification. *Rev. Mod. Phys.* **82**, 1155–1208 (2010). URL <https://link.aps.org/doi/10.1103/RevModPhys.82.1155>.

<sup>10</sup> Colangelo, G., Ciurana, F. M., Bianchet, L. C., Sewell, R. J. & Mitchell, M. W. Simultaneous tracking of spin angle and amplitude beyond classical limits. *Nature* **543**, 525–528 (2017). URL <http://dx.doi.org/10.1038/nature21434>.

<sup>11</sup> Shiga, N. & Takeuchi, M. Locking the local oscillator phase to the atomic phase via weak measurement. *New Journal of Physics* **14**, 023034 (2012).

<sup>12</sup> Degen, C. L., Poggio, M., Mamin, H. J., Rettner, C. T. & Rugar, D. Nanoscale magnetic resonance imaging. *Proc. Nat. Acad. Sci. U.S.A.* **106**, 1313 (2009). URL <http://dx.doi.org/10.1073/pnas.0812068106>.

<sup>13</sup> Ajoy, A., Bissbort, U., Lukin, M. D., Walsworth, R. L. & Cappellaro, P. Atomic-scale nuclear spin imaging using quantum-assisted sensors in diamond. *Phys. Rev. X* **5**, 011001 (2015).

<sup>14</sup> Perunicic, V. S., Hill, C. D., Hall, L. T. & Hollenberg, L. A quantum spin-probe molecular microscope. *Nat. Commun.* **7**, 12667 (2016). URL <http://dx.doi.org/10.1038/ncomms12667>.

<sup>15</sup> Weber, S. J. *et al.* Mapping the optimal route between two quantum states. *Nature* **511**, 570–573 (2014). URL <http://dx.doi.org/10.1038/nature13559>.

<sup>16</sup> Blok, M. S. *et al.* Manipulating a qubit through the back-action of sequential partial measurements and real-time feedback. *Nature Physics* **10**, 189 (2014).

<sup>17</sup> Bloembergen, N. & Pound, R. V. Radiation damping in magnetic resonance experiments. *Phys. Rev.* **95**, 8–12 (1954). URL <https://link.aps.org/doi/10.1103/PhysRev.95.8>.

<sup>18</sup> Sidles, J. A. Folded stern-gerlach experiment as a means for detecting nuclear magnetic resonance in individual nuclei. *Phys. Rev. Lett.* **68**, 1124–1127 (1992). URL <https://link.aps.org/doi/10.1103/PhysRevLett.68.1124>.

<sup>19</sup> Bergh, H. & McFarland, E. W. Nonlinear coupling and radiation damping in oscillator-detected magnetic resonance of single spins. *Meas. Sci. and Tech.* **7**, 1019 (1996).

<sup>20</sup> Berman, G. P., Borgonovi, F., Gorshkov, V. N. & Tsifrinovich, V. I. Modeling and simulations of a single-spin measurement using mrfm. *IEEE Transactions On Nanotechnology* **4**, 14–20 (2005).

<sup>21</sup> Taminiau, T. H., Cramer, J., van der Sar, T., Dobrovitski, V. V. & Hanson, R. Universal control and error correction in multi-qubit spin registers in diamond. *Nature Nano.* **9**, 171 (2014).

<sup>22</sup> Boss, J. M. *et al.* One- and two-dimensional nuclear magnetic resonance spectroscopy with a diamond quantum sensor. *Phys. Rev. Lett.* **116**, 197601 (2016).

<sup>23</sup> See *Supplementary Materials* accompanying this *manuscript*.

<sup>24</sup> Kalb, N. *et al.* Experimental creation of quantum Zeno subspaces by repeated multi-spin projections in diamond. *Nature Communications* **7**, 13111 (2016). URL <http://www.nature.com/doifinder/10.1038/ncomms13111>.

<sup>25</sup> Kohlhaas, R. *et al.* Phase locking a clock oscillator to a coherent atomic ensemble. *Phys. Rev. X* **5**, 021011 (2015).

<sup>26</sup> Slichter, C. P. *Principles of Magnetic Resonance, 3rd edition* (Springer, Berlin, 1990).

<sup>27</sup> Laraoui, A. *et al.* High-resolution correlation spectroscopy of c-13 spins near a nitrogen-vacancy centre in diamond. *Nature Commun.* **4**, 1651 (2013).

<sup>28</sup> Biercuk, M. J., Doherty, A. C. & Uys, H. Dynamical decoupling sequence construction as a filter-design problem. *Journal of Physics B - Atomic, Molecular and Optical Physics* **44**, 154002 (2011).

<sup>29</sup> Degen, C., Reinhard, F. & Cappellaro, P. Quantum sensing. *Rev. Mod. Phys.* **89**, 035002 (2017). URL <https://link.aps.org/doi/10.1103/RevModPhys.89.035002>.

<sup>30</sup> Schmitt, S. *et al.* Submillihertz magnetic spectroscopy performed with a nanoscale quantum sensor. *Science* **356**, 832 (2017).

<sup>31</sup> Boss, J. M., Cujia, K. S., Zopes, J. & Degen, C. L. Quantum sensing with arbitrary frequency resolution. *Science* **356**, 837–840 (2017).

<sup>32</sup> Glenn, D. R. *et al.* High-resolution magnetic resonance spectroscopy using a solid-state spin sensor. *Nature* **555**, 351 (2018). URL <http://dx.doi.org/10.1038/nature25781>.

<sup>33</sup> Shi, F. *et al.* Sensing and atomic-scale structure analysis of single nuclear-spin clusters in diamond. *Nature Physics* **10**, 21–25 (2014).

<sup>34</sup> Abobeih, M. H. *et al.* One-second coherence for a single electron spin coupled to a multi-qubit nuclear-spin environment. *arXiv:1801.01196* (2018). URL <https://arxiv.org/abs/1801.01196>.

<sup>35</sup> Alvarez, G. A. *et al.* Local and bulk c-13 hyperpolarization in nitrogen-vacancy-centred. *Nature Communications* **6**, 8456 (2015).

<sup>36</sup> Scheuer, J. *et al.* Optically induced dynamic nuclear spin polarisation in diamond. *New Journal Of Physics* **18**, 013040 (2016).

<sup>37</sup> Babinec, T. M. *et al.* A diamond nanowire single-photon source. *Nature Nano.* **5**, 195–199 (2010).

<sup>38</sup> Momenzadeh, S. A. *et al.* Nanoengineered diamond waveguide as a robust bright platform for nanomagnetometry using shallow nitrogen vacancy centers. *Nano Letters* **15**, 165–169 (2015). URL <http://dx.doi.org/10.1021/nl503326t>.

<sup>39</sup> Unden, T. *et al.* Coherent control of solid state nuclear spin nano-ensembles. *arXiv* **1802.02921** (2018). URL <https://arxiv.org/abs/1802.02921>.

<sup>40</sup> Rosskopf, T., Zopes, J., Boss, J. M. & Degen, C. L. A quantum spectrum analyzer enhanced by a nuclear spin memory. *NPJ Quantum Information* **3**, 33 (2017). URL <http://www.nature.com/articles/s41534-017-0030-6>.

## Supplementary Information

for the manuscript

“Watching the precession of a single nuclear spin by weak measurements”

K. S. Cujia, J. M. Boss, J. Zopes, and C. L. Degen

Department of Physics, ETH Zurich, Otto Stern Weg 1, 8093 Zurich, Switzerland

## Supplementary Note 1: Derivation of Spin Evolution and Measurement Back-action

To verify the simple Bloch vector picture of nuclear spin evolution, we calculate the quantum mechanical evolution of the coupled electron-nuclear system. We consider an ideal, closed two-spin system and neglect relaxation due to environmental couplings. The Hamiltonian of the coupled system, in the rotating frame of the electronic spin, is given by

$$\hat{H} = -\gamma_n \mathbf{B} \cdot \hat{\mathbf{I}} + \hat{\mathbf{S}} \cdot \mathbf{A} \cdot \hat{\mathbf{I}} \quad (\text{S1})$$

Here,  $\hat{\mathbf{S}}$  and  $\hat{\mathbf{I}}$  are the vectors containing the electron and nuclear spin operators, respectively,  $\gamma_n$  is the nuclear gyromagnetic ratio,  $\mathbf{B}$  is the external bias field, and  $\mathbf{A}$  is the hyperfine tensor. Although in our experiments the electronic spin is  $S = 1$ , we always work with the  $m_S = 0$  and  $m_S = -1$  spin-sublevels (whose transition energy is well separated from the  $m_S = 0$  to  $m_S = +1$  transition) that form an effective spin-1/2 system. Furthermore, assuming weak coupling between the electron and nuclear spins, we apply the secular approximation, leading to the Hamiltonian

$$\hat{H} = \hat{H}_0 + \hat{H}_{int} = -\omega_n \hat{I}_z + a_{\parallel} (\hat{S}_e + \hat{S}_z) \hat{I}_z + a_{\perp} (\hat{S}_e + \hat{S}_z) \hat{I}_x \quad (\text{S2})$$

where  $\hat{I}_x = \frac{1}{2}\sigma_x$ ,  $\hat{I}_z = \frac{1}{2}\sigma_z$  and  $\hat{S}_z = \frac{1}{2}(|0\rangle\langle 0| - |1\rangle\langle 1|) = \frac{1}{2}\sigma_z$  are the Pauli spin operators and  $\hat{I}_e = \hat{S}_e = \frac{1}{2}(|0\rangle\langle 0| + |1\rangle\langle 1|)$  are the identities. Before we proceed, we recall the Hausdorff formula for unitary propagation of the density matrix,

$$\hat{U} \rho \hat{U}^{\dagger} = e^{-i\hat{P}t} \hat{\rho} e^{i\hat{P}t} = \rho \cos(\sqrt{k}t) - \frac{i}{\sqrt{k}} \hat{Q} \sin(\sqrt{k}t) \quad (\text{S3})$$

where  $\hat{P}$  and  $\hat{Q}$  are operators,  $k$  is a scalar, and where  $[\hat{P}, \hat{\rho}] = \hat{Q}$  and  $[\hat{P}, \hat{Q}] = k\hat{\rho}$ .

We now calculate the effect of the first weak measurement. Starting with the sensor (electron) spin in the  $|0\rangle$  state and the nuclear spin in the  $|x\rangle$  state,

$$\hat{\rho} = \hat{\rho}_{s0} \otimes \hat{\rho}_{n0} = (\hat{S}_e + \hat{S}_z) (\hat{I}_e + \hat{I}_x) \quad (\text{S4})$$

We first apply a  $\pi/2$  pulse along  $\hat{S}_y$ ,

$$\rho = (\hat{S}_e + \hat{S}_x) (\hat{I}_e + \hat{I}_x)$$

Next we apply a sequence of  $N$  equidistant  $\pi$  pulses spaced by an interpulse delay  $2\tau$ . If the delay between the  $\pi$  pulses is adjusted to half the effective nuclear Larmor period, the system evolves under the effective Hamiltonian  $g2\hat{S}_z \hat{I}_x$  for a time  $t_{\beta} = N(2\tau)$ , where  $g = a_{\perp}/\pi$  is the coupling strength. Evolution under this Hamiltonian generates the conditional rotation around  $2\hat{S}_z \hat{I}_x$  with a rotation angle  $\beta = gt_{\beta} = a_{\perp}t_{\beta}/\pi$ . We call  $\beta$  the *measurement strength*. The corresponding propagator is  $U_{N\pi} = \exp(-\beta 2\hat{S}_z \hat{I}_x)$ . Using Eq. S3 (with  $\hat{P} = \hat{S}_z \hat{I}_x$ ,  $\sqrt{k} = 1/2$ ), application of the propagator yields

$$\hat{\rho} = (\hat{S}_e + \hat{S}_x \cos(\beta) + \hat{S}_y \sin(\beta)) (\hat{I}_e + \hat{I}_x)$$

Applying the second  $\pi/2$  pulse along  $\hat{S}_x$  we obtain

$$\hat{\rho} = (\hat{S}_e + \hat{S}_x \cos(\beta) + \hat{S}_z \sin(\beta)) (\hat{I}_e + \hat{I}_x)$$

Finally we perform a projective (optical) readout of the electronic spin. The optical readout measures  $\langle \hat{S}_z \rangle = \text{Tr}(\hat{\rho} \hat{S}_z) = \sin(\beta)/2$  and re-polarizes the sensor back on to the initial state  $\hat{\rho}_{s0}$ . We calculate the resulting nuclear state by tracing over the sensor spin,

$$\hat{\rho}_{n0} = \text{Tr}_e(\hat{\rho}) = (\hat{I}_e + \hat{I}_x) \quad (\text{S5})$$

We therefore conclude that a nuclear spin in the  $|x\rangle$  state is insensitive to a weak measurement.

Nuclear precession now takes place under  $\hat{H}_0 = -\omega_n \hat{I}_z$  (Eq. S2) for a time  $t_s$ , leading to a mixing of the  $\hat{I}_x$  and  $\hat{I}_y$  amplitudes,

$$\hat{\rho} = (\hat{S}_e + \hat{S}_z) (\hat{I}_e + \hat{I}_x \cos(\omega_n t_s) + \hat{I}_y \sin(\omega_n t_s)) \quad (\text{S6})$$

Using Eq. S3 and the following commutators, we calculate the outcome of the next weak measurement,

$$\begin{aligned} [\hat{S}_z \hat{I}_x, \hat{S}_x (\hat{I}_e + a \hat{I}_x)] &= i \frac{1}{2} \hat{S}_y (a \hat{I}_e + \hat{I}_x) ; \sqrt{k} = \frac{1}{2} \\ [\hat{S}_z \hat{I}_x, \hat{S}_x \hat{I}_y] &= \frac{i}{2} \{ \hat{S}_z, \hat{S}_x \} \hat{I}_z = 0 ; \sqrt{k} = \frac{1}{2} \\ [\hat{S}_z \hat{I}_x, \hat{S}_e \hat{I}_y] &= \frac{i}{2} \hat{S}_z \hat{I}_z ; \sqrt{k} = \frac{1}{2} \end{aligned}$$

The first  $\pi/2$  pulse along  $\hat{S}_y$  yields

$$\hat{\rho} = (\hat{S}_e + \hat{S}_x) (\hat{I}_e + \hat{I}_x \cos(\omega_n t_s) + \hat{I}_y \sin(\omega_n t_s))$$

Application of  $\hat{U}_{N\pi}$  results in

$$\begin{aligned} \hat{\rho} &= (\hat{S}_e + \hat{S}_x \cos(\beta)) (\hat{I}_e + \hat{I}_x \cos(\omega_n t_s)) \\ &+ \hat{S}_y \sin(\beta) (\hat{I}_e \cos(\omega_n t_s) + \hat{I}_x) \\ &+ (\hat{S}_e \cos(\beta) + \hat{S}_x) \hat{I}_y \sin(\omega_n t_s) + \hat{S}_z \hat{I}_z \sin(\omega_n t_s) \sin(\beta) \end{aligned}$$

The second  $\pi/2$  pulse along  $\hat{S}_x$  yields

$$\begin{aligned} \hat{\rho} &= (\hat{S}_e + \hat{S}_x \cos(\beta)) (\hat{I}_e + \hat{I}_x \cos(\omega_n t_s)) \\ &+ \hat{S}_z \sin(\beta) (\hat{I}_e \cos(\omega_n t_s) + \hat{I}_x) \\ &+ (\hat{S}_e \cos(\beta) + \hat{S}_x) \hat{I}_y \sin(\omega_n t_s) - \hat{S}_y \hat{I}_z \sin(\omega_n t_s) \sin(\beta) \end{aligned} \quad (\text{S7})$$

Optical readout again measures  $\langle \hat{S}_z \rangle$  and re-polarizes the sensor back on to the initial state  $\hat{\rho}_{s0}$ ,

$$\langle \hat{S}_z \rangle = \text{Tr}(\hat{\rho} \hat{S}_z) = \frac{1}{2} \cos(\omega_n t_s) \sin(\beta) \quad (\text{S8})$$

The effect of a single weak measurement now becomes more clear: it maps, proportionally to the measurement strength  $\sin(\beta) \approx \beta$ , the instantaneous nuclear  $\hat{I}_x$  amplitude onto the optically readable  $\langle \hat{S}_z \rangle$  component, while only weakly entangling the sensor and nuclear spins ( $\sin(\beta) \hat{S}_z \hat{I}_x$ ) such that a measurement of  $\hat{S}_z$  only partially projects the nuclear spin. The last term in Eq. S7 also indicates that the nuclear  $\hat{I}_z$  component develops an oscillatory correlation with the sensor  $\hat{S}_y$  component. Since the latter is never

measured, the nuclear spin does not experience, on average, a net rotation outside the precession plane. Furthermore, the information about this correlation becomes lost upon optical readout. We again calculate the partially projected nuclear state by tracing over the sensor spin

$$\hat{\rho}_{n1} = \hat{I}_e + \hat{I}_x \cos(\omega_n t_s) + \hat{I}_y \sin(\omega_n t_s) \cos(\beta) \quad (\text{S9})$$

$$= \hat{I}_e + a_1 \hat{I}_x + b_1 \hat{I}_y \quad (\text{S10})$$

where  $a_1$  and  $b_1$  are the respective amplitudes of  $\hat{I}_x$  and  $\hat{I}_y$ . The net effect of a single weak measurement on the nuclear spin is to scale the initial  $\hat{I}_y$  amplitude by a factor  $\cos(\beta)$ .

### Measurement-induced decoherence

We now apply a series of weak measurements. The next free precession period will again mix the  $\hat{I}_x$  and  $\hat{I}_y$  amplitudes

$$\begin{aligned} \hat{\rho} &= \left( \hat{S}_e + \hat{S}_z \right) \left( \hat{I}_e + (\cos(\omega_n t_s) \cos(\omega_n t_s) - \sin(\omega_n t_s) \cos(\beta) \sin(\omega_n t_s)) \hat{I}_x \right. \\ &\quad \left. + (\cos(\omega_n t_s) \sin(\omega_n t_s) + \sin(\omega_n t_s) \cos(\beta) \cos(\omega_n t_s)) \hat{I}_y \right) \\ &= \left( \hat{S}_e + \hat{S}_z \right) \left( \hat{I}_e + a_2 \hat{I}_x + b_2 \hat{I}_y \right) \end{aligned}$$

and the subsequent weak measurement will again scale the resulting  $\hat{I}_y$  amplitude by a factor  $\cos(\beta)$ . The nuclear state after the  $n$ 'th readout is

$$\begin{aligned} \hat{\rho}_n(n) &= \hat{I}_e + \hat{I}_x a_n + \hat{I}_y b_n \\ &= \hat{I}_e + \hat{I}_x (a_{n-1} \cos(\omega_n t_s) - b_{n-1} \sin(\omega_n t_s)) \\ &\quad + \hat{I}_y (a_{n-1} \sin(\omega_n t_s) + b_{n-1} \cos(\omega_n t_s)) \cos(\beta) \end{aligned} \quad (\text{S11})$$

with  $a_0 = 1$  and  $b_0 = 0$ . We next develop recursion relations (Eq. S11) for the  $\hat{I}_x$  and  $\hat{I}_y$  amplitudes

$$\begin{aligned} a_0 &= 1 \\ a_1 &= \cos(\omega_n t_s) \\ a_2 &= \cos^2(\omega_n t_s) - \sin^2(\omega_n t_s) \cos(\beta) \\ &= \frac{1}{2} \cos(\omega_n(2t_s))(1 + \cos(\beta)) + \frac{1}{2}(1 - \cos(\beta)) \\ a_3 &= \left( \frac{1}{2} \cos(\omega_n(2t_s))(1 + \cos(\beta)) + \frac{1}{2}(1 - \cos(\beta)) \right) \cos(\omega_n t_s) \\ &\quad - \left( \frac{1}{2} \sin(\omega_n(2t_s))(1 + \cos(\beta)) \cos(\beta) \right) \sin(\omega_n t_s) \\ &= \frac{1}{4} \cos(\omega_n(3t_s))(1 + \cos(\beta))^2 + (1 - \cos(\beta)) \cos(\omega_n t_s) \left( \frac{1}{2} + \frac{1}{4}(1 + \cos(\beta)) \right) \\ a_4 &= \frac{1}{8} \cos(\omega_n(4t_s))(1 + \cos(\beta))^3 + (1 - \cos(\beta)) \left( \frac{1}{2} \cos(\omega_n(2t_s))(1 + \cos(\beta)) + \frac{1}{8}(3 + \cos^2(\beta)) \right) \\ a_n &= \frac{1}{2^{n-1}} \cos(\omega_n(nt_s)) (1 + \cos(\beta))^{n-1} + (1 - \cos(\beta)) f_{an}(\dots) \end{aligned}$$

$$\begin{aligned}
b_0 &= 0 \\
b_1 &= \sin(\omega_n t_s) \cos(\beta) \\
b_2 &= \cos(\omega_n t_s) \sin(\omega_n t_s) (1 + \cos(\beta)) \cos(\beta) \\
&= \frac{1}{2} \sin(\omega_n(2t_s)) (1 + \cos(\beta)) \cos(\beta) \\
b_3 &= \left( \frac{1}{2} \cos(\omega_n(2t_s)) (1 + \cos(\beta)) + \frac{1}{2} (1 - \cos(\beta)) \right) \sin(\omega_n t_s) \cos(\beta) \\
&\quad + \left( \frac{1}{2} \sin(\omega_n(2t_s)) (1 + \cos(\beta)) \cos(\beta) \right) \cos(\omega_n t_s) \cos(\beta) \\
&= \frac{1}{4} \sin(\omega_n(3t_s)) \cos(\beta) (1 + \cos(\beta))^2 + (1 - \cos(\beta)) \cos(\beta) \sin(\omega_n t_s) \left( \frac{1}{2} - \frac{1}{4} (1 + \cos(\beta)) \right) \\
b_4 &= \frac{1}{8} \sin(\omega_n(4t_s)) \cos(\beta) (1 + \cos(\beta))^3 + \frac{1}{4} (1 - \cos(\beta))^2 \cos(\beta) (1 + \cos(\beta)) \sin(\omega_n(2t_s)) \\
b_n &= \frac{1}{2^{n-1}} \sin(\omega_n(nt_s)) \cos(\beta) (1 + \cos(\beta))^{n-1} + (1 - \cos(\beta)) f_{bn}(\dots)
\end{aligned}$$

where  $f_{an,bn}(\dots)$  are polynomial functions which depend on  $\cos(\beta)$  and on the parity of  $n \in \mathbb{N}$ .

$$\begin{cases} f_{an,bn}(\cos(\beta), \cos(\omega_n(2m)t_s)); m \in [0 \dots n/2], & n \text{ even} \\ f_{an,bn}(\cos(\beta), \cos(\omega_n(2m+1)t_s)); m \in [0 \dots (n-1)/2], & n \text{ odd.} \end{cases}$$

For weak measurements, i.e.  $\beta \ll 1$ , the polynomials  $f_{an,bn}(\dots) \approx \mathcal{O}(1)$  and  $(1 - \cos(\beta)) \approx 0 + \mathcal{O}(\beta^2)$ . We can therefore approximate the amplitudes as

$$\begin{aligned}
a_n &\approx \cos(\omega_n(nt_s)) \left( \frac{1 + \cos(\beta)}{2} \right)^{n-1} \\
b_n &\approx \sin(\omega_n(nt_s)) \cos(\beta) \left( \frac{1 + \cos(\beta)}{2} \right)^{n-1}
\end{aligned}$$

We observe that both amplitudes correspond to quadratures which oscillate at the precession frequency  $\omega_n$  and become scaled by a power of  $\cos(\beta)$ . Expanding  $\cos(\beta)$  to second order and using the binomial expansion we find

$$\left( \frac{1 + \cos(\beta)}{2} \right)^{n-1} \approx \left( 1 - \frac{\beta^2}{4} \right)^m = \sum_{n=0}^m \binom{m}{n} (1)^{m-n} (-1)^n \left( \frac{\beta^2}{4} \right)^n$$

where we have set  $m = n - 1$ . To observe the approximate scaling of this term at the  $n$ 'th readout, we assume the limit of a large number of readouts  $m$  and use Stirling's formula to approximate the factorials

$$\sum_{n=0}^m \binom{m}{n} (1)^{m-n} (-1)^n \left( \frac{\beta^2}{4} \right)^n \approx \sum_{n=0}^m \frac{m^n}{n!} (-1)^n \left( \frac{\beta^2}{4} \right)^n = \sum_{n=0}^m \frac{1}{n!} \left( \frac{-m\beta^2}{4} \right)^n \approx e^{-m\beta^2/4} \quad (\text{S12})$$

The scaling for the nuclear state follows the form

$$\hat{\rho}_n(t) \approx \hat{I}_e + \left( \hat{I}_x \cos(\omega_n t) + \hat{I}_y \sin(\omega_n t) \right) e^{-\Gamma_\beta t} + \mathcal{O}(\beta^2) \quad (\text{S13})$$

where  $t = n \cdot t_s$ ;  $n \in \mathbb{N}$  with  $t_s$  being the sampling period and  $\Gamma_\beta = \beta^2/(4t_s)$ . For  $t \rightarrow \infty$ ,  $\rho_n \rightarrow \hat{I}_e$ . Hence, the net effect of a series of weak measurements is an exponential decay of the nuclear coherences  $\hat{I}_x$  and  $\hat{I}_y$

at a measurement-induced rate  $\Gamma_\beta$  proportional to the square of the measurement strength, ultimately leading to a fully mixed state. From Eq. S12 we observe that the number of measurements that can be performed before the nuclear spin dephases (defined as a  $1/e$  decay) is  $n = 4/\beta^2$ . Alternatively the dephasing time is

$$T_\beta = \frac{1}{\Gamma_\beta} = \frac{4}{\beta^2} t_s$$

Any nuclear spin will also have some intrinsic dephasing  $\Gamma_0 = (T_{2,n}^*)^{-1}$  given by the intrinsic dephasing time  $T_{2,n}^*$ . The total decay rate is then the sum of all contributions

$$\Gamma = \Gamma_\beta + \Gamma_0$$

### Frequency synchronization

We now turn our attention to the validity of our approximations for Eq. S13. We first consider the case when the effective sampling time approximates a half or a full Larmor period. Such a scenario corresponds to the case when we continuously measure the nuclear spin when it finds itself along the  $X$  (or  $Y$ ) axes in the Bloch sphere. We thus go back to Eq. S11 and set

$$\omega_n t_s = 2\pi \left( \frac{T/2 \pm \delta t}{T} \right) = \pi \pm \frac{2\pi\delta t}{T} = \pi \pm \delta\alpha$$

where  $T$  is the Larmor period and  $\delta t \ll T$  is the detuning in the sampling period  $t_s$  from half a Larmor period. From Eq. S11, the nuclear state at the  $k_{th}$  readout becomes

$$\begin{aligned} \hat{\rho}_n(n) &= \hat{I}_e + \left( \hat{I}_x (a_{n-1} \cos(\delta\alpha) - b_{n-1} \sin(\delta\alpha)) + \hat{I}_y (a_{n-1} \sin(\delta\alpha) + b_{n-1} \cos(\delta\alpha)) \cos(\beta) \right) \cos(\pi) \\ &\approx \hat{I}_e + \left( \hat{I}_x \left( a_{n-1} \left( 1 - \frac{\delta\alpha^2}{2} \right) - b_{n-1} \delta\alpha \right) + \hat{I}_y \left( a_{n-1} \delta\alpha + b_{n-1} \left( 1 - \frac{\delta\alpha^2}{2} \right) \right) \cos(\beta) \right) \cos(\pi) + \mathcal{O}(\delta\alpha^3) \end{aligned}$$

Developing the recursion for the amplitudes  $a_n$  and  $b_n$  with  $a_0 = 1$  and  $b_0 = 0$ , we find

$$\begin{aligned} a_0 &= 1 \\ a_1 &= -\left( 1 - \frac{\delta\alpha^2}{2} \right) \\ a_2 &= 1 - \delta\alpha^2 (1 + \cos(\beta)) \\ a_3 &= -\left( 1 - \delta\alpha^2 \left( \frac{1}{2} + (1 + \cos(\beta))^2 \right) \right) \\ a_n &= (-1)^n \left( 1 - \delta\alpha^2 f_{an}(\cos(\beta)) \right) + \mathcal{O}(\delta\alpha^3) \end{aligned}$$

$$\begin{aligned} b_0 &= 0 \\ b_1 &= -\delta\alpha \cos(\beta) \\ b_2 &= \delta\alpha \cos(\beta) (1 + \cos(\beta)) \\ b_3 &= -\delta\alpha \cos(\beta) (1 + \cos(\beta)) (1 + \cos(\beta)) \\ b_n &= (-1)^n \delta\alpha \cos(\beta) f_{bn}(\cos(\beta)) + \mathcal{O}(\delta\alpha^3) \end{aligned}$$

where  $f_{an,bn}$  are polynomial functions of order  $n$  on  $\cos(\beta)$ . The nuclear state is therefore

$$\hat{\rho}_n(n) \approx \hat{I}_e + \left( \hat{I}_x (1 - \delta\alpha^2 f_{an}(\cos(\beta))) + \hat{I}_y (\delta\alpha \cos(\beta) f_{bn}(\cos(\beta))) \right) \cos(n\pi)$$

as the product  $\delta\alpha \cos(\beta) \rightarrow 0$ , the nuclear state becomes

$$\hat{\rho}_n(n) \approx \hat{I}_e + \hat{I}_x \cos(n\pi) = \hat{I}_e + \hat{I}_x \cos((0.5\omega_s)t_s) \quad (\text{S14})$$

where  $\omega_s = 2\pi t_s^{-1}$ . Eq. (S14) reveals that we effectively observe a state which remains unaffected by the measurements and is precessing at (half) the sampling frequency, and not at its Larmor frequency. For an increasing detuning  $\delta\alpha$ , we only observe this effect for stronger measurements, *i.e.*, for  $\beta \rightarrow \pi/2$ , where the measurement becomes increasingly projective. In this case, the product  $\delta\alpha \cos(\beta) \rightarrow 0$  and we approach the behavior of Eq. S14. It is easy to see that for an effective sampling time close to the Larmor period, *i.e.*  $t_s \approx T$ , the behavior is completely analogous and the nuclear state would be

$$\hat{\rho}_n(n) \approx \hat{I}_e + \hat{I}_x \cos(\omega_s t_s) \quad (\text{S15})$$

### Nuclear spin z-component

In our analysis we have assumed a nuclear spin with zero  $\hat{I}_z$  component. It is nevertheless important to note what the evolution for a finite  $\hat{I}_z$  polarization looks like. From Eq. S4 we observe that the presence of a finite nuclear spin  $\hat{I}_z$  component right before a measurement leads to an additional term in the system density matrix of the form

$$\propto (\hat{S}_e + \hat{S}_x) (\hat{I}_z)$$

To observe the measurement effect on this component, we first calculate the commutators

$$\begin{aligned} [\hat{S}_z \hat{I}_x, \hat{S}_x \hat{I}_z] &= -\frac{i}{2} \{ \hat{S}_z, \hat{S}_x \} \hat{I}_y = 0 \\ [\hat{S}_z \hat{I}_x, \hat{S}_e \hat{I}_z] &= -\frac{i}{2} \hat{S}_z \hat{I}_y \end{aligned}$$

The weak measurement transforms this component according to Eq. S3 (with  $\sqrt{k} = 1/4$ )

$$\propto (\hat{S}_e + \hat{S}_x) (\hat{I}_z) \rightarrow \hat{S}_e \hat{I}_z \cos(\beta) - \hat{S}_z \hat{I}_y \sin(\beta) + \hat{S}_x \hat{I}_z$$

The second  $\pi/2$  pulse on the sensor spin followed by optical readout therefore yield a partially projected nuclear state of the form

$$\hat{S}_e \hat{I}_z \cos(\beta) + \hat{S}_y \hat{I}_y \sin(\beta) + \hat{S}_x \hat{I}_z \rightarrow \hat{I}_z \cos(\beta)$$

Larmor precession only rotates the in-plane components, so an  $\hat{I}_z$  component of a precessing nuclear spin upon  $n$  weak measurements evolves in analogy to its  $\hat{I}_y$  component without the effect of Larmor precession.

$$\hat{I}_z \cos(\beta) \rightarrow \hat{I}_z (\cos(\beta))^n \approx (\hat{I}_z) e^{-n\beta^2/2}$$

The nuclear  $\hat{I}_z$  component therefore experiences a measurement-induced exponential decay at double the rate of the in-plane components. As indicated in Eq. S12, the slower decay rate for in-plane spin components is due to Larmor precession.

## Supplementary Note 2: Signal-to-Noise Ratio

We estimated the signal-to-noise ratio (SNR) of the weak measurement technique and compared it to the SNR of a corresponding experiment using a strong measurement.

For our SNR estimation, we assume that the output noise is dominated by the shot noise of the optical readout (and not by quantum projection noise), which is a typical situation for experiments with NV centers. The SNR per unit time is then given by the ratio between the differential photon count  $\delta C_{\text{tot}}$  (the signal) and the square root of the total photon counts  $C_{\text{tot}}$  (the noise), normalized to the total measurement time  $T_{\text{tot}}$ ,

$$\text{SNR} = \frac{\delta C_{\text{tot}}}{\sqrt{C_{\text{tot}} T_{\text{tot}}}} \quad (\text{S16})$$

Here,  $\delta C_{\text{tot}}$  corresponds to the change in optical intensity that is proportional to the meter spin's  $\hat{S}_z$  state, and  $C_{\text{tot}}$  corresponds to the total intensity that determines the shot noise. To compare the SNRs for weak and strong measurements, we calculate  $\delta C_{\text{tot}}$ ,  $C_{\text{tot}}$  and  $T_{\text{tot}}$  for both experiments.

### Weak measurement experiment

Our weak measurement experiment consists of an initialization step that prepares the nuclear spin in the  $\hat{I}_x$  state, followed by  $n$  weak measurements separated by a sampling time  $t_s$ . The duration of a single repetition of the experiment is given by

$$T_{\text{tot}} = t_{\text{init}} + n t_s \quad (\text{S17})$$

where  $t_{\text{init}}$  is the time it takes to initialize the nuclear spin into  $\hat{I}_x$ . The total counts are given by

$$C_{\text{tot}} = n C_0 \quad (\text{S18})$$

where  $C_0$  is the photon count of one optical readout. The differential photon count of the  $j$ 'th weak measurement is given by

$$\delta C_j = \frac{1}{2} \epsilon C_0 \sin \beta e^{-\Gamma_e t_\beta} e^{-j \Gamma t_s} \quad (\text{S19})$$

$$\approx \frac{1}{2} \epsilon C_0 \beta e^{-\Gamma_e t_\beta} e^{-j \Gamma t_s} = \frac{1}{2} \epsilon C_0 g t_\beta e^{-\Gamma_e t_\beta} e^{-j \Gamma t_s} \quad (\text{S20})$$

where  $\epsilon$  is the optical intensity contrast,  $\beta = g t_\beta$  is the measurement strength,  $g$  is the coupling constant,  $t_\beta$  is the interaction time, and  $\Gamma_e = 1/T_{2,e}$  is the electronic decoherence rate that is effective during  $t_\beta$ . The approximation  $\sin \beta \approx \beta \ll \pi/2$  acknowledges that the measurement is weak.  $\Gamma$  is the nuclear dephasing rate,

$$\Gamma = \Gamma_0 + \Gamma_\beta = \Gamma_0 + \frac{g^2 t_\beta^2}{4 t_s} \quad (\text{S21})$$

which is the sum of the intrinsic dephasing rate  $\Gamma_0$  and the measurement-induced dephasing rate  $\Gamma_\beta = \beta^2/(4 t_s)$  (see Supplementary Note 1). The total differential photon count is the sum over all  $\delta C_j$ ,

$$\delta C_{\text{tot}} = \sum_{j=1}^n \delta C_j \approx \frac{\epsilon C_0 g t_\beta e^{-\Gamma_e t_\beta} (1 - e^{-n \Gamma t_s})}{2 \Gamma t_s} \quad (\text{S22})$$

where we have replaced the sum by an integral and performed the integration. The SNR is then given by

$$\text{SNR}_{\text{weak}} = \frac{\delta C_{\text{tot}}}{\sqrt{C_{\text{tot}} T_{\text{tot}}}} = \frac{\epsilon \sqrt{C_0} g t_{\beta} e^{-\Gamma_{\text{e}} t_{\beta}} (1 - e^{-n \Gamma t_{\text{s}}})}{2 \Gamma t_{\text{s}} \sqrt{n(t_{\text{init}} + n t_{\text{s}})}} \quad (\text{S23})$$

We now simplify this SNR by making the following assumptions:

- The initialization time is much shorter than the duration of free precession,  $t_{\text{init}} \ll n t_{\text{s}}$ .
- Because the interrogation time  $t_{\beta}$  is relatively short, there is no decoherence of the electronic sensor spin during  $t_{\beta}$ , and  $e^{-\Gamma_{\text{e}} t_{\beta}} \approx 1$ .
- The sensor readout/reset time is short compared to the interrogation time  $t_{\beta}$ , such that  $t_{\text{s}} \approx t_{\beta}$ .

These assumptions will need to be justified for a specific experimental setting. The simplified SNR is

$$\text{SNR}_{\text{weak}} \approx \frac{1}{2} \epsilon \sqrt{C_0 g} \frac{1 - e^{-n \Gamma t_{\beta}}}{n \Gamma \sqrt{t_{\beta}}} \quad (\text{S24})$$

The two free experimental parameters in this SNR are the interaction time  $t_{\beta}$  and the number of measurements  $n$ . The choice of  $t_{\beta}$  and  $n$  that maximizes the SNR is given by the condition

$$n \Gamma t_{\beta} \approx 1 \quad (\text{S25})$$

or equivalently,  $n t_{\beta} \approx T_{2,n}^*$ . Eq. (S25) indicates that one should make the measurement duration  $n t_{\text{s}}$  approximately equal to the nuclear dephasing time  $T_{2,n}^* = \Gamma^{-1}$ . Note that  $\Gamma$  depends itself on  $t_{\beta}$  because of Eq. (S21). To choose an interaction time  $t_{\beta}$ , we therefore demand that  $\Gamma \approx 2\Gamma_0$ , *i.e.*, that the measurement-induced decay rate  $\Gamma_{\beta}$  is similar to the intrinsic dephasing rate  $\Gamma_0$ ,

$$t_{\beta}(\Gamma_{\beta} = \Gamma_0) = \frac{4\Gamma_0}{g^2} \quad (\text{S26})$$

Evaluation of Eqs. (S24-S26) yields the optimum SNR (up to a factor of order unity)

$$\text{SNR}_{\text{weak}}^{(\text{opt})} \approx \epsilon \sqrt{C_0 \Gamma_0} \quad (\text{S27})$$

### Strong measurement experiment

For comparison, we calculate the SNR that is achievable using strong measurements. Our comparison experiment consists of  $n$  separate acquisitions with progressively longer free precession times  $t_j = j t_{\text{s}}$  where  $j = 1 \dots n$ . Each acquisition consists of an initialization step, rotation of the nuclear spin to  $\hat{I}_x$ , a free precession of duration  $t_j$ , and a strong measurement of the  $\hat{I}_x$  component. The time trace is then assembled from the  $n$  separate measurement outputs. The total time spent on the experiment is

$$T_{\text{tot}} = n t_{\text{init}} + \sum_{j=1}^n j t_{\text{s}} = n \left[ t_{\text{init}} + \frac{1}{2} (n+1) t_{\text{s}} \right] \quad (\text{S28})$$

where the duration of the strong measurement (equal to the duration needed to perform a rotation by  $\beta = \pi/2$ ) has been included in  $t_{\text{init}}$ . The total photon count is given by

$$C_{\text{tot}} = n C_0 \quad (\text{S29})$$

The differential photon count is given by

$$\delta C_j = \frac{1}{2} \epsilon C_0 \sin \beta^* e^{-\Gamma_e t_\beta^*} e^{-j\Gamma_0 t_s} \quad (\text{S30})$$

where the nuclear dephasing rate  $\Gamma$  is now equal to the intrinsic dephasing rate  $\Gamma_0$ .  $\beta^*$  is the rotation angle of the strong measurement, which ideally is  $\beta^* = \pi/2$ , unless the electronic decoherence (given by  $\Gamma_e$ ) prevents a strong measurement.  $t_\beta^* = \beta^*/g$  is the associated interrogation time of the strong measurement. The total differential photon count becomes

$$\delta C_{\text{tot}} = \sum_{j=1}^n \delta C_j \approx \frac{\epsilon C_0 \sin \beta^* e^{-\Gamma_e t_\beta^*} (1 - e^{-n\Gamma_0 t_s})}{2\Gamma_0 t_s} \quad (\text{S31})$$

The SNR is given by

$$\text{SNR}_{\text{strong}} = \frac{\delta C_{\text{tot}}}{\sqrt{C_{\text{tot}} T_{\text{tot}}}} = \frac{\epsilon \sqrt{C_0} \sin \beta^* e^{-\Gamma_e t_\beta^*} (1 - e^{-n\Gamma_0 t_s})}{2\Gamma_0 t_s n \sqrt{t_{\text{init}} + \frac{1}{2}(n+1)t_s}} \quad (\text{S32})$$

We now apply the same simplifications to the SNR as in the weak measurement case. First, we assume that  $t_{\text{init}} \ll nt_s$ . Second, we assume that  $n$  is large such that  $n+1 \approx n$ . Note that  $t_\beta^* \gg t_s$  because the duration of a strong measurement is comparably long. The simplified SNR is

$$\text{SNR}_{\text{strong}} \approx \frac{\epsilon \sqrt{C_0} \sin \beta^* e^{-\Gamma_e t_\beta^*} (1 - e^{-n\Gamma_0 t_s})}{\sqrt{2}\Gamma_0 (nt_s)^{3/2}} \quad (\text{S33})$$

To compare the strong and weak measurement SNRs, we choose the same  $n$  and  $t_s$  values for both measurements. For weak measurements,  $nt_s\Gamma \approx 1$  according to Eq. (S25). For strong measurements,  $nt_s\Gamma_0 \approx 0.5$  because the nuclear decay rate for strong measurements is half that of the weak measurement case,  $\Gamma_0 = \Gamma/2$ . The SNR becomes

$$\text{SNR}_{\text{strong}} \approx \epsilon \sqrt{C_0 \Gamma_0} \sin \beta^* e^{-\Gamma_e t_\beta^*}, \quad (\text{S34})$$

again up to a factor of order unity. Clearly, this SNR is identical to the weak measurement  $\text{SNR}_{\text{weak}}$ , Eq. (S27), except for the  $t_\beta^*$ -dependent factors. For a situation where a strong measurement is possible,  $\sin(gt_\beta^*) \approx 1$  and  $e^{-\Gamma_e t_\beta^*} \approx 1$ , and the weak and strong measurement SNRs are approximately equal,

$$\text{SNR}_{\text{strong}} \approx \epsilon \sqrt{C_0 \Gamma_0} \approx \text{SNR}_{\text{weak}} \quad \text{for } gT_{2,e} > 1 \quad (\text{S35})$$

Conversely, if the coupling  $g$  is too weak to enable a strong measurement,  $\sin(gt_\beta^*) \approx gT_{2,e}$ , and the weak measurement outperforms the strong measurement,

$$\text{SNR}_{\text{strong}} \approx gT_{2,e} \epsilon \sqrt{C_0 \Gamma_0} \ll \text{SNR}_{\text{weak}} \quad \text{for } gT_{2,e} < 1 \quad (\text{S36})$$

### Supplementary Data 3: Experimental Parameters

#### Parameters of NV centers and $^{13}\text{C}$ nuclear spin

NV	$g (2\pi \text{ kHz})$	$a_{\parallel} (2\pi \text{ kHz})$	$a_{\perp} (2\pi \text{ kHz})$	$T_{2,\text{CPMG}} (\mu\text{s})$
1	46.78	-18.61	146.35	42
2	4.651	0.540	14.61	165
3	54.22	16.78	150.75	21
4	33.41	381.21	113.29	35
5	37.18	41.56	117.53	500

TABLE S1: Hyperfine coupling parameters calculated for the nuclear spins associated to each NV center. Following Ref. [1], the parallel coupling  $a_{\parallel}$  is determined from a free precession experiment yielding two frequencies whose difference is approximately  $a_{\parallel}$ . The transverse coupling  $a_{\perp}$  is obtained by driving a nuclear Rabi oscillation via the electronic spin, and recording the oscillation frequency  $f_R$ , where  $a_{\perp}/(2\pi) = \pi f_R$ . We extract these frequencies from the measurements shown in Fig. S4 to Fig. S14.

#### Parameters for Figures 2

NV center	1
B field	191.8 mT
NV initialization laser pulse	1.5 $\mu\text{s}$
NV readout laser pulse	1.5 $\mu\text{s}$
$\pi/2$ rotation CPMG pulses	24
$\pi/2$ rotation CPMG duration	5.908 $\mu\text{s}$
Weak measurement CPMG pulses $K$	{1, 2, 4, 6, 8, 12, 16}
Weak measurement CPMG duration $t_{\beta}$	{0.246, 0.493, 0.985, 1.477, 1.969, 2.954, 3.938} $\mu\text{s}$
Sampling period $t_s$	{3.24, 3.24, 3.76, 4.24, 5.00, 5.72, 7.20} $\mu\text{s}$
Number of weak measurements $n$	61
Integration time	{1496, 691, 661, 628, 675, 481, 391} sec

### Parameters for Figures 3

<i>Figure 3a</i>	
NV center	3
B field	190.8 mT
NV initialization laser pulse	$1.5 \mu s$
NV readout laser pulse	$1.5 \mu s$
$\pi/2$ rotation CPMG pulses	24
$\pi/2$ rotation CPMG duration	$5.874 \mu s$
Weak measurement CPMG pulses $K$	2
Weak measurement CPMG duration $t_\beta$	$0.489 \mu s$
Sampling period $t_s$	$(3.56 + j 0.01) \mu s; j \in \mathbb{N} = [0, 49]$
Number of weak measurements $n$	51
<i>Figure 3b,c</i>	
NV center	5
B field	194 mT
NV initialization laser pulse	$1.5 \mu s$
NV readout laser pulse	$1.5 \mu s$
$\pi/2$ rotation CPMG pulses	32
$\pi/2$ rotation CPMG duration	$7.579 \mu s$
Weak measurement CPMG pulses $K$	$\{2, 6, 12\}$
Weak measurement CPMG duration $t_\beta$	$\{0.474, 1.422, 2.844\} \mu s$
Sampling period $t_s$	$\{3.061, 4.013, 4.956\} + j 0.002 \mu s; j \in \mathbb{N} = [0, 48]$
Number of weak measurements $n$	49
<i>Figure 3d</i>	
NV center	5
B field	194 mT
NV initialization laser pulse	$1.5 \mu s$
NV readout laser pulse	$1.5 \mu s$
$\pi/2$ rotation CPMG pulses	32
$\pi/2$ rotation CPMG duration	$7.579 \mu s$
Weak measurement CPMG pulses $K$	12
Weak measurement CPMG duration $t_\beta$	$2.844 \mu s$
Sampling period $t_s$	$5.933 + j 0.001 \mu s; j \in \mathbb{N} = [0, 48]$
Number of weak measurements $n$	49

### Parameters for Figure 4

NV center	2
B field	190.2 mT
NV initialization laser pulse	$1.5 \mu\text{s}$
NV readout laser pulse	$1.5 \mu\text{s}$
$\pi/2$ rotation CPMG pulses	176
$\pi/2$ rotation CPMG duration	$43.384 \mu\text{s}$
Weak measurement CPMG pulses $K$	16
Weak measurement CPMG duration $t_\beta$	$3.944 \mu\text{s}$
Sampling period $t_s$	$13.92 \mu\text{s}$
Number of weak measurements $n$	501

### Parameters for Supplementary Figure S2

NV center	4
B field	190 mT
NV initialization laser pulse	$1.5 \mu\text{s}$
NV readout laser pulse	$1.5 \mu\text{s}$
$\pi/2$ rotation CPMG pulses	$\{4, 8, 12, 16, 24, 32\}$
$\pi/2$ rotation CPMG duration	$\{0.822, 1.764, 2.647, 3.523, 5.294, 7.058\} \mu\text{s}$
Strong measurement CPMG pulses $K$	32
Strong measurement CPMG duration $t_\beta$	$7.058 \mu\text{s}$

## Supplementary Figure 1: Extended Pulse Diagram

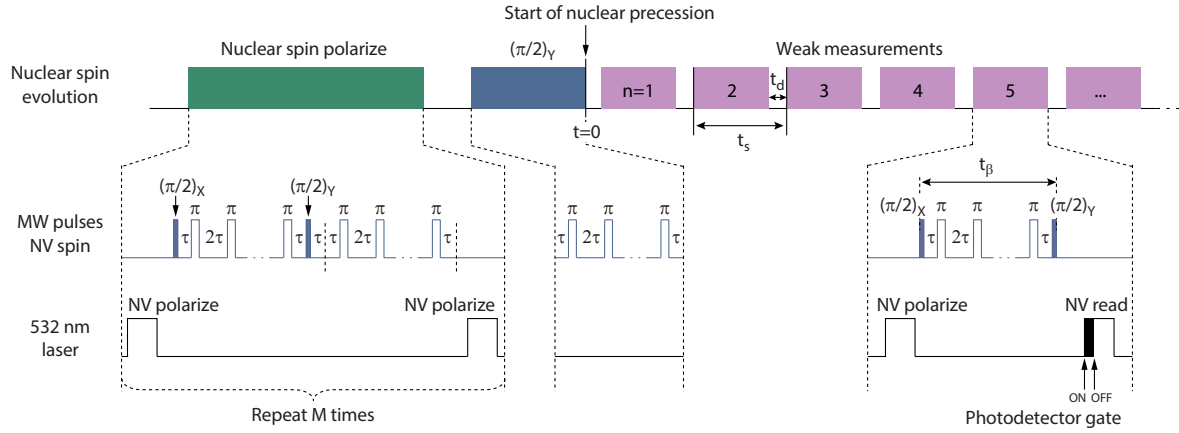


**FIG. S1: Extended pulse-timing diagram.** The sensor is initially polarized by means of a  $\sim 532$  nm laser pulse. We subsequently apply a polarization transfer gate [2] in a repetitive fashion. From the nuclear spin perspective, the polarization sequence consists of a  $\pi/2$  conditional X-rotation, followed by a  $\pi/2$  Z-rotation and a subsequent  $\pi/2$  conditional X-rotation. We implement the conditional X-rotations as a resonant Carr-Purcell-Meiboom-Gill (CPMG) decoupling sequence applied on the electronic spin. The CPMG sequences consist of a periodic train of microwave  $\pi$  pulses with alternating phases and an interpulse delay of  $2\tau$ . The CPMG sequence is resonant when the interpulse delay matches the effective Larmor frequency of the nuclear spin,  $\tau \approx \pi/(2(\omega_0 + 0.5a_{\parallel}))$ , where  $a_{\parallel}$  is the parallel dipolar hyperfine coupling between the sensor and the nuclear spin. This condition leads to an effective interaction between the sensor and nuclear spin of the form  $g 2\hat{S}_z \hat{I}_x$  [1, 3], *i.e.*, a simultaneous conditional rotation, where  $g = a_{\perp}/\pi$  is a coupling rate determined by the transverse dipolar hyperfine coupling between the sensor and the nuclear spin. We implemented Z-rotations as a waiting time of length  $\pi/2\omega_0$  if the sensor was polarized into  $m_S = 0$ , or of length  $\tau$  if it was not. Z-rotations can alternatively be implemented as non-resonant CPMG sequences, which effectively decouple the evolution of the nuclear spin from the sensor [2]. To initiate precession, we apply a  $\pi/2$  Y-rotation on the nuclear spin, implemented as another  $\pi/2$  X-rotation followed by a  $\pi/2$  Z-rotation. We then probed the nuclear state X-projection,  $\langle \hat{I}_x \rangle$ , at intervals of a sampling time  $t_s$  by means of weak measurements. Each weak measurement instance was implemented as a resonant CPMG decoupling sequence of duration  $t_{\beta}$ , sandwiched between two  $\pi/2$  pulses whose axes were orthogonal, here X and Y. We used a laser pulse to readout the sensor  $\hat{S}_z$  state upon each weak measurement instance. An additional delay time  $t_d$  was used to adjust the sampling time  $t_s$ . For simplicity we have neglected the length of our microwave pulses, nevertheless in practice their finite duration needs to be taken into account when designing the described nuclear rotations. It is worth noting that the X and Y rotation axes for the sensor spin are in general not the same as those for the nuclear spin. While the former are set by the phase of the first applied microwave pulse (rotating frame picture), the latter are defined by the dipolar hyperfine coupling, with the XZ plane being that between  $a_{\perp}$  and the nuclear quantization axis (in our case set by the external bias field).

## Supplementary Figure 2: Repetitive Initialization of Nuclear Spin

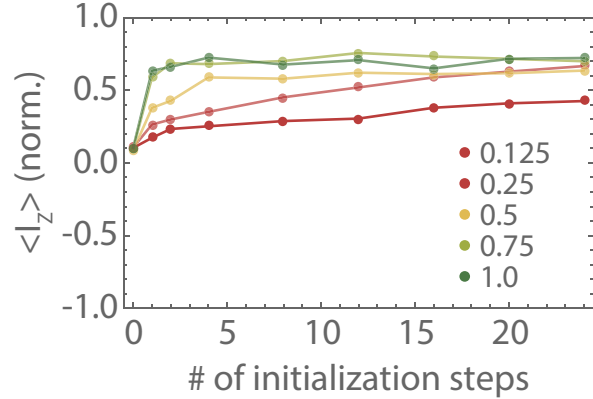


FIG. S2: **Nuclear spin polarization as a function of repeated initialization cycles.** The associated protocol is explained in Fig. S1. The plot shows the degree of nuclear spin polarization  $\langle \hat{I}_z \rangle$  versus the number of repetitions of the initialization protocol. We measured  $\langle \hat{I}_z \rangle$  using spin tomography [2]. Different colors represent different angles for the conditional X-rotations, varied from  $\pi/2$  (green dots) to  $0.125(\pi/2)$  (red dots). The plot demonstrates that even for incomplete X-rotations, polarization transfer from the NV center to the nuclear spin can still be achieved. This is relevant for a very weakly coupled nuclear spin, where the electron coherence time is too short to perform full  $\pi/2$  X-rotations.

**Supplementary Figure 3: Measured Precession Frequency vs. Free Precession Frequency**

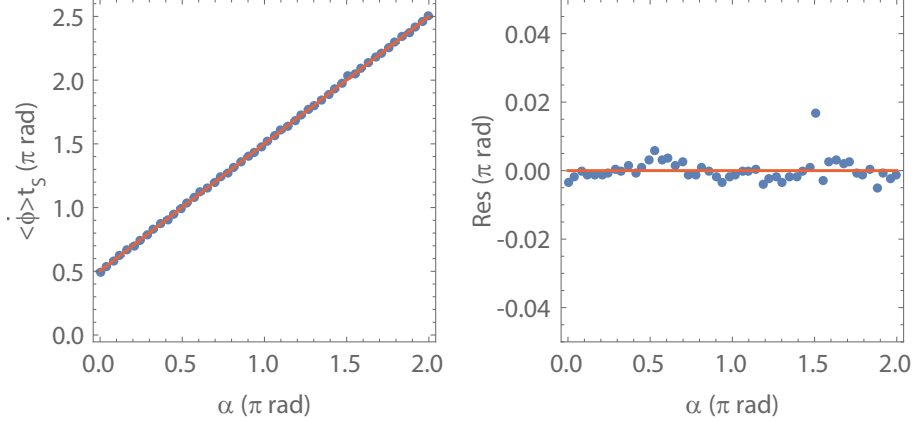


FIG. S3: **Measured Precession Frequency vs. Free Precession Frequency.** (a) Signal frequency extracted from Lorentzian fits to each spectrum in Fig. 3a. We fit a linear function  $ax + b$  and find  $a = 0.999305 \pm 0.000789$ ,  $b = 0.002171 \pm 0.000916$ . A  $\chi^2$  test yields  $\chi^2 = 0.000325$  and a corresponding  $p\text{-val} = 1.0$  according to the  $\chi^2$  distribution for  $k = 50$  measurement points. (b) Residuals for the linear fit in (a). Frequency synchronization is absent in this plot because of the weak measurement strength ( $\beta \sim 8^\circ$ ).

## Supplementary Figures for NV 1

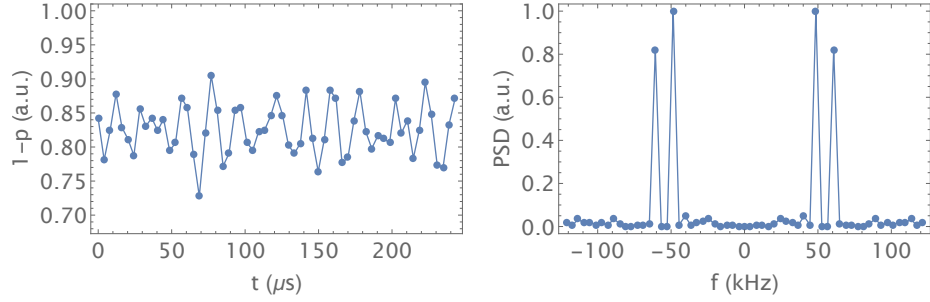


FIG. S4: Correlation spectroscopy for NV1.  $t_s = 4.084 \mu s$

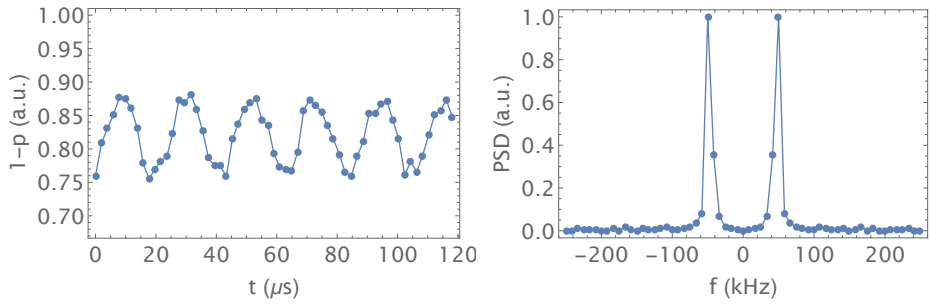


FIG. S5: Correlation spectroscopy with induced nuclear rabi rotation during waiting time for NV1.  $t_s = 1.969 \mu s$

## Supplementary Figures for NV 2

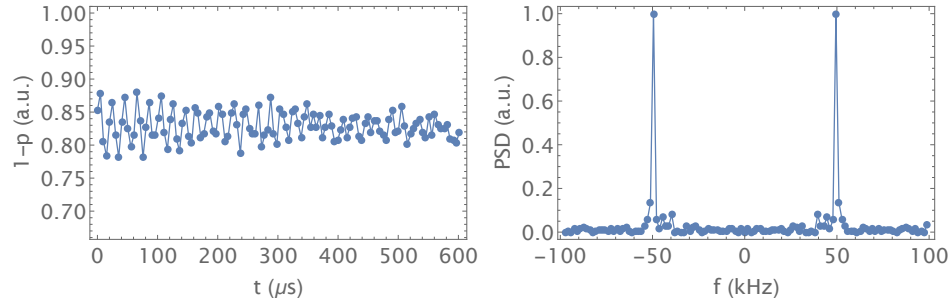


FIG. S6: Correlation spectroscopy for NV2.  $t_s = 5.054 \mu s$

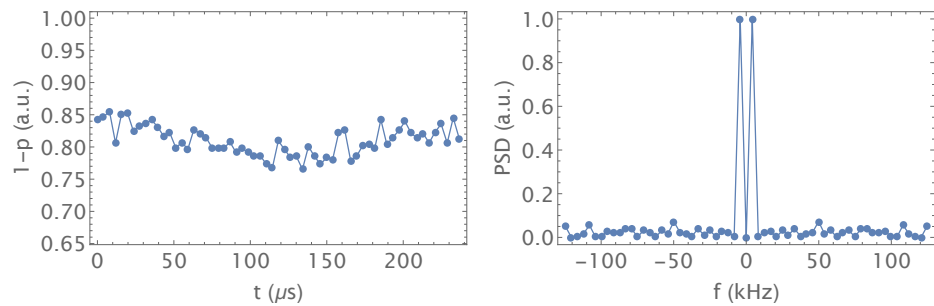


FIG. S7: Correlation spectroscopy with induced nuclear rabi rotation during waiting time for NV2.  $t_s = 3.944 \mu s$

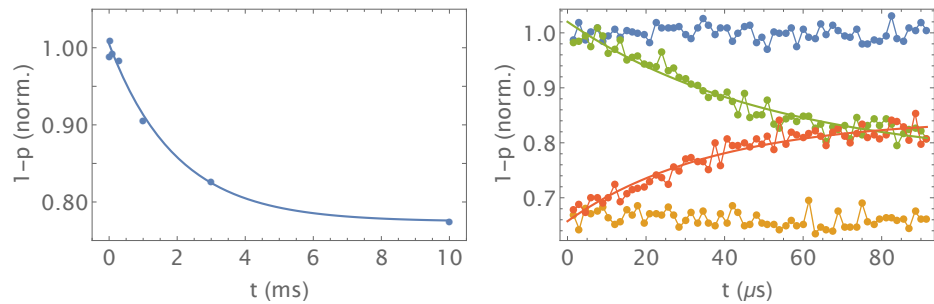


FIG. S8:  $T_1$  relaxation time (left) and  $T_2$  (right). Solid lines are exponential fits yielding  $T_1 = 1.97 \text{ ms}$  and  $T_{2,\text{cho}} = 52.6 \mu s$

## Supplementary Figures for NV 3

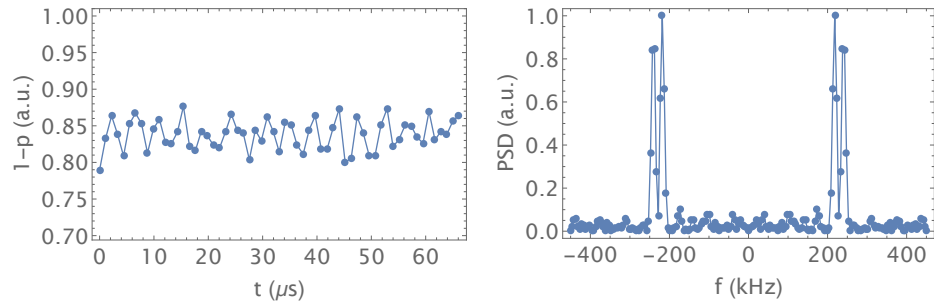


FIG. S9: Correlation spectroscopy for NV3.  $t_s = 1.102 \mu s$

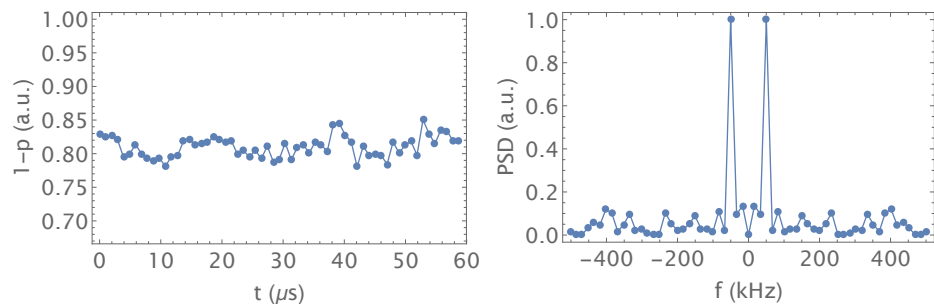


FIG. S10: Correlation spectroscopy with induced nuclear rabi rotation during waiting time for NV3.  $t_s = 0.979 \mu s$

## Supplementary Figures for NV 4

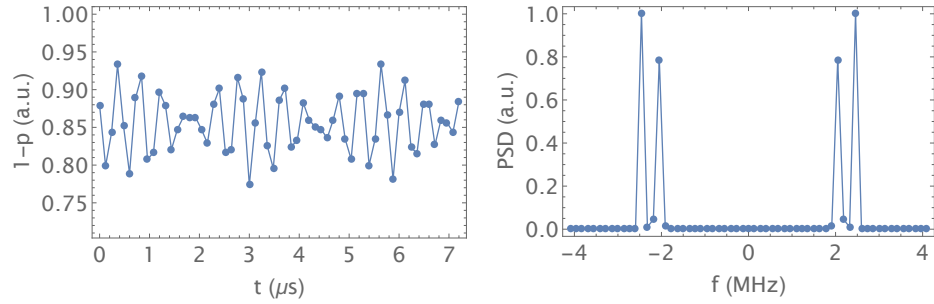


FIG. S11: Correlation spectroscopy for NV4.  $t_s = 0.120 \mu\text{s}$

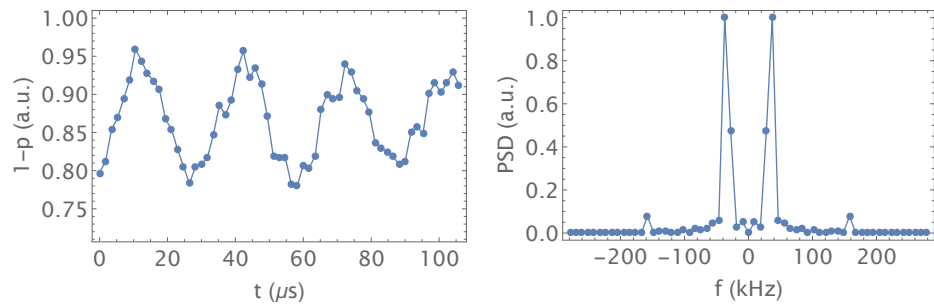


FIG. S12: Correlation spectroscopy with induced nuclear rabi rotation during waiting time for NV4.  $t_s = 1.764 \mu\text{s}$

## Supplementary Figures for NV 5

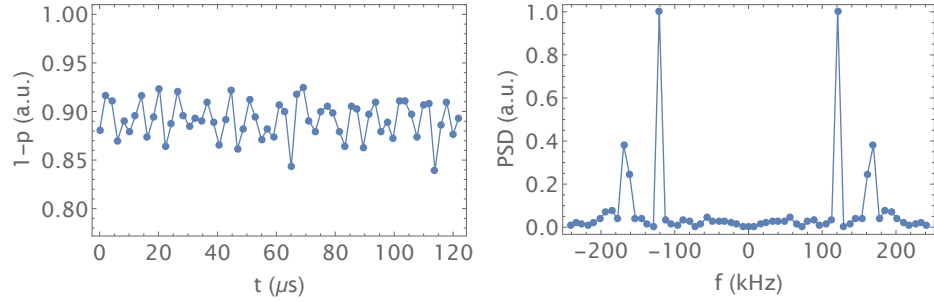


FIG. S13: Correlation spectroscopy for NV5.  $t_s = 2.033 \mu\text{s}$

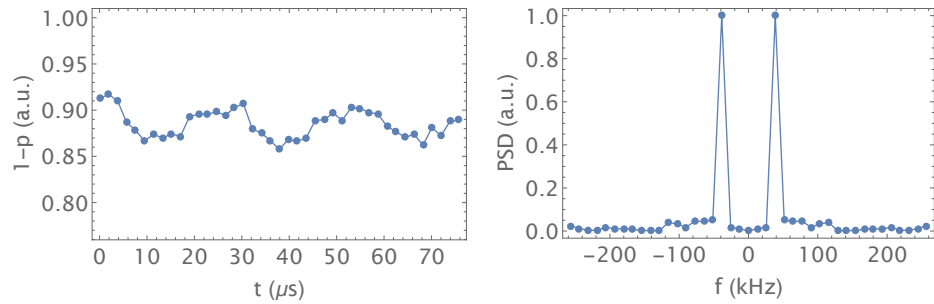


FIG. S14: Correlation spectroscopy with induced nuclear rabi rotation during waiting time for NV5.  $t_s = 1.895 \mu\text{s}$

## References

---

- [1] J. M. Boss, K. Chang, J. Armijo, K. Cujia, T. Rosskopf, J. R. Maze, and C. L. Degen, Phys. Rev. Lett. **116**, 197601 (2016).
- [2] T. H. Taminiau, J. Cramer, T. van der Sar, V. V. Dobrovitski, and R. Hanson, Nature Nano. **9**, 171 (2014).
- [3] T. H. Taminiau, J. J. T. Wagenaar, T. V. der Sar, F. Jelezko, V. V. Dobrovitski, and R. Hanson, Phys. Rev. Lett. **109**, 137602 (2012).